Turbulence subject to axisymmetric expansion generated by opposed multiple jet arrays

Zexu Han,[1] Tomoaki Watanabe,[1]† and Koji Nagata[1]

[1]Department of Mechanical Engineering and Science, Kyoto University, Kyoto 615-8540, Japan

(Received xx; revised xx; accepted xx)

Turbulence subject to axisymmetric expansion is experimentally investigated using opposed multiple-jet arrays. For each array, jet interaction generates decaying, nearly homogeneous and isotropic turbulence within a duct. The turbulent flows from the opposed arrays collide and spread radially, forming a mean-flow stagnation point with associated mean strain. Flow properties are examined using particle image velocimetry. The mean velocity gradient tensor, $A_{ij} = \partial\langle u_i\rangle/\partial x_j$, satisfies $A_{xx} : A_{yy} : A_{zz} = -2 : 1 : 1$ with $A_{xx} < 0$, indicating axisymmetric expansion. Turbulence is strongly influenced by this expansion, becoming increasingly anisotropic toward the stagnation point, suggesting a cumulative effect of mean strain. The ratios of streamwise to transverse root-mean-square velocity fluctuations, $u_{\mathrm{rms}}/v_{\mathrm{rms}}$, and of their integral scales both increase relative to an isotropic state, consistent with rapid distortion theory (RDT). However, because the strain time scale is comparable to that of large-scale motions, deviations from RDT arise, including larger $u_{\mathrm{rms}}/v_{\mathrm{rms}}$ values and a steeper decay of energy spectra in the inertial subrange than the $-5/3$ law. The spectral slope change is opposite to that reported for axisymmetric contraction, suggesting a common mechanism for spectral modification in both strain types, since both are described by the same tensor form with opposite signs of A_{ij}. Consistently, the scaling exponents of velocity structure functions differ from predictions based on Kolmogorov's second similarity hypothesis, even for low-order functions. These results confirm that axisymmetric mean strain significantly modifies turbulence properties, some of which are considered universal for other turbulent flows.

1. Introduction

Turbulence in the presence of a mean velocity gradient is a fundamental problem relevant to many flows in physics and engineering. Internal flows with varying cross-section experience mean strain arising from streamwise variation of the mean velocity (Ayyalasomayajula & Warhaft 2006). Mean strain also plays an important role in the flow near stagnation points around bluff bodies (Li *et al.* 2024). Another important example is turbulence under mean

† Email address for correspondence: watanabe.tomoaki.8x@kyoto-u.ac.jp

shear, as observed in jets, wakes and boundary layers. The mean velocity gradient tensor $\boldsymbol{A}$ is defined as

$$\boldsymbol{A} = \begin{pmatrix} \partial\langle u\rangle/\partial x & \partial\langle u\rangle/\partial y & \partial\langle u\rangle/\partial z \\ \partial\langle v\rangle/\partial x & \partial\langle v\rangle/\partial y & \partial\langle v\rangle/\partial z \\ \partial\langle w\rangle/\partial x & \partial\langle w\rangle/\partial y & \partial\langle w\rangle/\partial z \end{pmatrix}, \tag{1.1}$$

where u, v and w are the velocity components in the x, y and z directions, respectively, and $\langle\cdot\rangle$ denotes an average. Hereafter, vector and tensor components are denoted by subscripts corresponding to the x, y and z directions; for example, $A_{xx} = \partial u/\partial x$. Fundamental studies of turbulence often consider specific forms of A_{ij}. For example, simple mean shear corresponds to A_{ij} having a single non-zero off-diagonal component, with all other components equal to zero. Other cases involve irrotational mean strains, characterised by the diagonal components of A_{ij}. A typical example is axisymmetric strain, which can be classified into two forms: axisymmetric contraction and axisymmetric expansion, represented by

$$\boldsymbol{A} = \begin{pmatrix} S & 0 & 0 \\ 0 & -S/2 & 0 \\ 0 & 0 & -S/2 \end{pmatrix} \quad \text{for axisymmetric contraction,} \tag{1.2}$$

and

$$\boldsymbol{A} = \begin{pmatrix} -S & 0 & 0 \\ 0 & S/2 & 0 \\ 0 & 0 & S/2 \end{pmatrix} \quad \text{for axisymmetric expansion,} \tag{1.3}$$

with strain rate $S > 0$. The distinction between these two forms is illustrated by the deformation of a fluid element. Under axisymmetric contraction, a spherical element is elongated along the symmetry axis and compressed in the transverse directions, forming a rugby-ball-like shape. In contrast, under axisymmetric expansion, the element is compressed along the axis and stretched transversely, forming a flattened, pancake-like shape. Mean deformation due to shear and strain, described by $\boldsymbol{A}$, influences turbulence through production, dissipation, redistribution of turbulent kinetic energy across scales and space and the development of anisotropy (Keffer 1965; Pope 2000). The effects of mean deformation on initially homogeneous and isotropic turbulence (HIT) have long been central topics in fluid mechanics.

Axisymmetric irrotational strain is of particular interest because it represents one of the simplest anisotropic forms of A_{ij} (Sagaut & Cambon 2018). Statistical axisymmetry enables the development of theories for strained homogeneous turbulence. A notable example is rapid distortion theory (RDT), which assumes that mean strain acts on turbulence over a time scale much shorter than that of the turbulent motions. RDT has been employed to predict the evolution of initially HIT subjected to a sudden imposition of axisymmetric contraction or expansion (Batchelor & Proudman 1954; Lee 1989). Related theoretical works address statistically axisymmetric turbulence without mean strain, which are applicable when turbulence is exposed to axisymmetric strain for a finite duration and subsequently evolves freely in its absence. These theoretical frameworks build upon the kinematics of axisymmetric turbulence (Batchelor 1946; Chandrasekhar 1950; Lindborg 1995). Other theories consider the decay of homogeneous axisymmetric turbulence (Davidson *et al.* 2012) and predict decay laws under the influence of external forces such as buoyancy in stably stratified fluids or the Coriolis force due to rotation (Davidson 2010, 2013; Watanabe *et al.* 2022).

Turbulence subject to axisymmetric strain has also been studied using direct numerical simulations (DNS) and experiments. In DNS, uniform mean strain is introduced by deforming the computational domain (Rogallo 1981). This method has been used to investigate the evolution of turbulence under a finite duration of axisymmetric contraction or expansion,

followed by relaxation without strain (Zusi & Perot 2014; Clay & Yeung 2016). Similar simulations have also been conducted for planar strain (Chen *et al.* 2006; Zusi & Perot 2013). DNS has also been used to explore the behaviour of particles seeded in turbulence subject to axisymmetric expansion (Gylfason *et al.* 2011). Relevant wind tunnel experiments have been carried out for grid-generated turbulence passing through a contracting section, where the streamwise variation of tunnel cross-section induces axisymmetric contraction (Uberoi 1956). Turbulence is strongly modified while traversing the contracting section, followed by relaxation in the downstream region of constant cross-section. Many experimental investigations have thus focused on axisymmetric contraction (Hussain & Ramjee 1976; Sjögren & Johansson 1998; Ayyalasomayajula & Warhaft 2006; Ertunç & Durst 2008; Alhareth *et al.* 2024). Other related examples include experiments on turbulence subject to planar contraction, in which the mean strain consists of expansion and contraction along two orthogonal directions (Thoroddsen & Van Atta 1995; Brown *et al.* 2006; Mugundhan *et al.* 2020). Experimental studies on axisymmetric expansion are far fewer than those on contraction. One example of axisymmetric expansion is grid turbulence passing through a diverging section (Choi & Lumley 2001). Another example utilises a facility comprising two opposing discs moving towards each other in a water tank (Liu *et al.* 1999; Hassanian *et al.* 2023).

Most experimental studies on turbulence subject to axisymmetric strain have focused on contraction. Investigations of turbulence subject to axisymmetric contraction have consistently shown that non-linear effects play a major role in the influence of mean strain, leading to deviations from RDT predictions. The measured energy spectrum exhibits increasingly pronounced departures from RDT at higher Reynolds numbers (Ayyalasomayajula & Warhaft 2006), highlighting the importance of high-Reynolds-number investigations for clarifying the effects of mean strain. However, previous laboratory studies of axisymmetric expansion have predominantly been conducted at lower Reynolds numbers. The present study introduces a new facility that realises turbulence subject to axisymmetric expansion at high Reynolds numbers. The facility comprises two multiple-jet generators, each producing decaying, nearly HIT through jet interaction. The opposed jet arrays generate two turbulent flows that collide and form a mean-flow stagnation point, thereby establishing axisymmetric strain. The role of the two arrays is to establish axisymmetric expansion in the stagnation region from initially nearly homogeneous, isotropic inflows generated by each array. A turbulent flow issuing from a single jet nozzle exhibits a highly inhomogeneous transverse distribution of velocity statistics. By contrast, interaction among many jets within a confined test section forms nearly HIT, with velocity statistics homogeneous across the cross-sectional planes (Tan *et al.* 2023; Mori *et al.* 2024). This configuration is consistent with theories and numerical simulations that explore mean-strain effects on initially isotropic turbulence and is well suited to examine departures from isotropy caused by mean strain. The multiple-jet generator is identical to that used in our previous studies (Mori *et al.* 2024; Watanabe *et al.* 2024, 2025), where the formation and decay of nearly HIT were characterised using particle image velocimetry (PIV). In those works, the turbulent Reynolds number based on the Taylor microscale reached values as high as 750, exceeding those attained in earlier experiments on turbulence subject to axisymmetric expansion.

In the present study, we perform PIV measurements to characterise turbulence under axisymmetric expansion. Because high-speed jet interaction generates high-Reynolds-number turbulence, the present data are well suited to assess the effects of axisymmetric expansion on inertial-range scalings of velocity fluctuations, which have not been examined in previous studies. Previous studies on turbulence subject to axisymmetric expansion primarily addressed anisotropy via one-point statistics; Reynolds-number limitations hindered discussion of spectral and structure-function behaviour. The present results demonstrate anisotropy

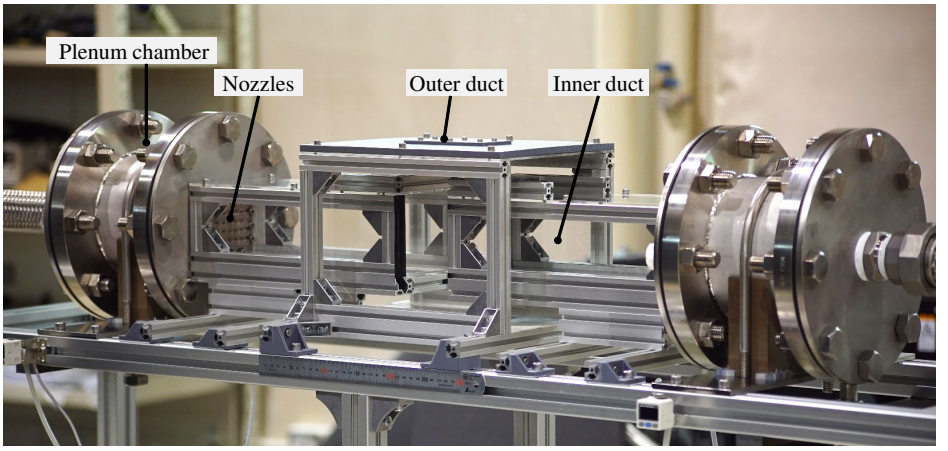

Figure 1: Photograph of the OMJA facility.

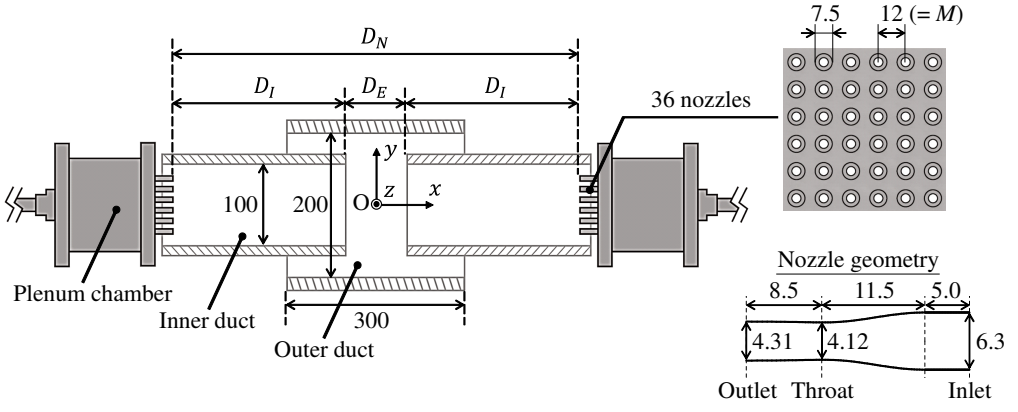

Figure 2: Schematic of the OMJA facility. All dimensions are in mm. All components appear in pairs except the outer duct. The inner ducts have a square cross-section of 100^2 mm^2. The outer duct has a square cross-section of 200^2 mm^2 and length 300 mm. Coordinates x, y and z denote the jet-flow, vertical and lateral directions, respectively. Each plenum chamber is equipped with 6×6 Laval nozzles with inlet, throat and outlet diameters of 6.3 mm, 4.12 mm and 4.31 mm, respectively. The spacing between adjacent nozzles is $M = 12$ mm, and the nozzle outer diameter is 7.5 mm. The inner-duct length and the nozzle-to-nozzle spacing between the two jet arrays are denoted by D_I and D_N, which determine the gap between the inner-duct ends as $D_E = D_N - 2D_I$.

introduced by the expansion and reveal deviations in energy spectra and structure functions from predictions based on RDT or Kolmogorov's second similarity hypothesis.

The paper is organised as follows. Section 2 describes the turbulence facility and the measurement techniques. Section 3 presents the experimental results, including the mean flow field and statistical properties of velocity fluctuations. Finally, the main findings are summarised in § 4.

2. Experimental setup and measurement methods

2.1. *Opposed multiple-jet array facility*

The Opposed Multiple-Jet Array (OMJA) facility consists of two multiple-jet generators and a test section. A photograph of the OMJA is shown in figure 1, and its schematic is illustrated in figure 2. The jet direction is denoted by x, the vertical direction by y and the remaining direction by z. A total of 6×6 jets are issued from each generator into the inner ducts. These jets interact and evolve into nearly HIT as they pass through the ducts, as reported in our previous study (Mori *et al.* 2024). Here, in wind-tunnel experiments of decaying HIT, "homogeneous" typically refers to the cross-sectional plane, while streamwise inhomogeneity persists due to decay (Comte-Bellot & Corrsin 1966). The opposed turbulent flows collide near the centre of the test section after exiting the inner ducts, spread radially toward the outer duct, and then discharge from the section. The inner and outer ducts have square cross-sections of 100×100 mm^2 and 200×200 mm^2, respectively. The collision of the opposed flows generates a mean strain field around the test-section centre. As shown below, the mean strain comprises compression in the x direction and expansion in the y and z directions, approximating axisymmetric expansion. As the turbulent flows from the opposing jet arrays approach the test-section centre and then proceed toward the outer duct, they experience the mean strain for longer durations, leading to accumulated-strain effects. Consequently, in the present set-up the flow is expected to be inhomogeneous. Velocity measurements are conducted in the central region to characterise turbulence influenced by the mean strain. The facility details are described below.

Two identical jet generators and air-supply systems are placed on either side of the test section. Compressed air is stored in two 400 L tanks (Anest Iwata, SAT-400C-140) pressurised by oil-free compressors (Anest Iwata, TFP75CF-10). The compressed air is dried and cooled by refrigerant-type dryers (Orion Machinery, RAX8J-SE-A1) before entering the tanks. Downstream of the tanks, the pneumatic system comprises moisture separators (SMC, AF800-14), pressure regulators (SMC, AR825-14G) and solenoid valves (SMC, VXP2380-14-5G). When the solenoid valves are opened, compressed air at the regulated pressure is supplied to each plenum chamber. All pipes and fittings between the tanks and chambers have a nominal size of JIS 40A, corresponding to an inner diameter of approximately 40 mm.

Each jet generator consists of a plenum chamber made from a stainless-steel pipe with an inner diameter of 155.2 mm and a length of 160 mm. Two chambers are mounted on a single aluminium frame, allowing adjustment of their positions in the x direction. One end of each chamber is connected to the air supply system via a stainless-steel flange, and the endplate facing the test section is fitted with a nozzle plate containing 6×6 Laval nozzles. The endplate also features a pressure port connected to pressure sensors. The internal geometry of the nozzle is shown in figure 2. The nozzle inlet, throat and outlet diameters are 6.3 mm, 4.12 mm and 4.31 mm, respectively. The first 5 mm from the inlet has a constant diameter of 6.3 mm. The diameter in the convergent section is reduced to 4.12 mm at the throat over 11.5 mm following a cosine function of the streamwise location. In a diverging section, the diameter increases to 4.31 mm at the outlet. The diameter profile in the diverging section is determined analytically (Foelsch 1949). The nozzles are designed to produce fully expanded supersonic jets with a Mach number $M_J = U_J/a_J = 1.36$ and a jet Reynolds number $Re_J = \rho_J U_J D/\mu_J = 1.9 \times 10^5$ at a plenum pressure of 300 kPa, where $U_J = 404$ m/s is the jet velocity, $D = 4.31$ is the jet exit diameter, $a_J = 297$ m/s is the speed of sound, $\rho_J = 1.61$ kg/m^3 is the density, and $\mu_J = 1.44 \times 10^{-5}$ Pa·s is the kinematic viscosity. These fluid properties refer to the flow state at the nozzle outlet and is determined based on the nozzle design. The spacing between adjacent nozzles is $M = 12$ mm, and the outer nozzle diameter is 7.5 mm, as shown in figure 2. The nozzle plate is fixed to the plenum chamber

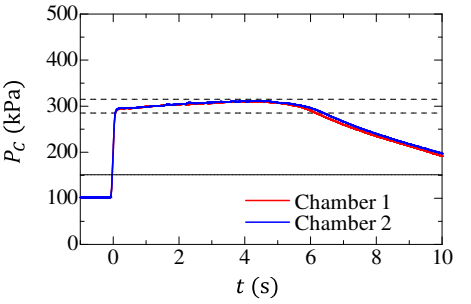

Figure 3: Variations in plenum pressure P_C in each plenum chamber. Horizontal dashed lines indicate ±5% of 300 kPa, for which the nozzles are designed to produce ideally expanded supersonic jets. The horizontal solid line denotes 151.2 kPa, the critical pressure above which the exit Mach number is independent of plenum pressure. The time origin (t = 0) corresponds to the instant when the pressure reaches 200 kPa. Signals are smoothed using a moving average with a window of 0.1 s.

endplate using seal washers, nuts and a 1 mm-thick PTFE gasket sheet to prevent leakage. We define the reference velocity and length scales for turbulence generation as the jet velocity U_J and the jet spacing M, which are used to normalise the results.

All technical specifications of the jet generators, including the plenum chambers and nozzles, are identical to those in our previous studies on decaying HIT generated by jet interaction from a single jet array (Mori *et al.* 2024; Watanabe *et al.* 2024, 2025), except for a minor adjustment of chamber size in the present setup. Although the jets are initially supersonic, mixing with the surrounding fluid significantly reduces the mean velocity. Consequently, both mean velocity and fluctuations are much lower than the speed of sound except in the near-nozzle region, and compressibility effects are locally negligible once jet interaction forms decaying nearly HIT.

The test section consists of inner and outer ducts. Two inner ducts with a square cross-section of 100×100 mm^2 are attached to the plenum chamber endplates. Jet interaction within each inner duct generates nearly HIT, which decays with distance from the nozzles. From the gap between the inner-duct ends, the turbulent flow enters a 300 mm-long outer duct with a square cross-section of 200×200 mm^2. Both ducts are constructed from clear acrylic walls supported by aluminium frames. The top wall of the outer duct contains small closable holes for inserting sensors for pressure and temperature measurements. The inner-duct length, D_I, and the nozzle-to-nozzle spacing between the two jet arrays, D_N, are key experimental parameters. These define the gap between the duct ends as $D_E = D_N - 2D_I$. The geometric parameters are illustrated in figure 2, and their values are given below. They are varied by exchanging inner-duct components of different lengths and by adjusting the plenum chamber positions.

2.2. *Experimental conditions*

Prior to each experiment, the air tanks are pressurised to approximately 0.9 MPaG. Once the solenoid valves are opened, compressed air from the tanks is supplied to the plenum chambers, raising the plenum pressure. The pressure regulators are adjusted such that the plenum pressure is maintained at approximately 300 kPa, at which each nozzle is designed to generate fully expanded supersonic jets with $M_J = 1.36$ and $Re_J = 1.9 \times 10^5$. In our previous study, based on Schlieren visualisation and the Prandtl formula (Pack 1950), the actual jet Mach number was estimated to be about 1.33, consistent with the nozzle design (Mori *et al.* 2024).

Upon opening the valves, 6×6 jets are issued from the nozzle arrays of both generators. The plenum pressures P_C in the two chambers are measured simultaneously using pressure sensors (SMC, PSE540), and the signals are recorded with an oscilloscope (Yokogawa, DL850E) at 5 kHz. Figure 3 shows the pressure variation during a representative run. Immediately after valve opening, the pressure rises rapidly to $P_C \approx 300$ kPa. Up to $t \approx 5$ s, it continues to increase gradually due to the mechanical characteristics of the regulators, a phenomenon known as the supply pressure effect. The horizontal dashed lines indicate $\pm 5\%$ of 300 kPa. During the first 6 s, the pressure remains within this range. After $t \approx 6$ s, it decreases due to the pressure drop in the tanks. Accordingly, the flows are regarded as statistically steady during the initial 6 s, within which all measurements are conducted. The pressure difference between the two chambers remains negligible in this period, ensuring that both generators produce jets with the same characteristics. For the present nozzle design, the jet velocity at the nozzle outlet is independent of plenum pressure once it exceeds 151.2 kPa, as indicated by the horizontal solid line. The root-mean-square (rms) plenum-pressure fluctuation over the first 6 s is 7 kPa, which is sufficiently small that the jet velocity remains constant. Plenum-pressure fluctuations do, however, affect the static pressure and density at the nozzle outlet: for a 7 kPa fluctuation, both vary by about 2 %. These variations lead to 2 % fluctuations in the jet Reynolds number, indicating that jet properties hardly vary with time. This estimate is based on a one-dimensional nozzle-flow analysis and does not consider other effects such as wall influences inside the nozzle. Our previous study of the same jet array presented Schlieren visualisation of the jet, which showed that the Mach disc forming from the nozzle outlet is steady in time (Mori *et al.* 2024). The visualisation also indicates small temporal variations in the jet properties.

Table 1 lists the tested values of D_I, D_N and D_E, together with measurement results discussed in § 3. These values are normalised by the jet spacing M in table 1. Different geometric parameters are chosen to vary the characteristics of the strain and turbulence. Jet interaction forms nearly HIT, which decays in the mean flow direction within the inner duct (Mori *et al.* 2024). The inner-duct length D_I is set to exceed $25M$. The velocity fluctuations become statistically homogeneous in the cross-sectional plane before $25M$ downstream of the nozzles. As turbulence decays, the integral scale representing the characteristic size of large-scale motions increases. At large streamwise distances this growth leads to confinement effects from the test-section walls, manifested as accelerated decay of turbulent kinetic energy and inhibited scale growth (Skrbek & Stalp 2000; Morize & Moisy 2006), which become prominent beyond $50M$ (Watanabe *et al.* 2025). Accordingly, the maximum D_I is set below $50M$. When the flows from the two generators reach the ends of the inner ducts, a stagnation point forms in the mean flow due to their interaction, with the mean velocity in the x direction decreasing towards this point. Since the velocity gradient depends on the distance from the inner-duct end to the stagnation point, experiments are conducted with different gaps D_E between $6.7M$ and $10.0M$ adjusted by varying D_I according to $D_E = D_N - 2D_I$. Consequently, a small change in D_I markedly affects D_E: from case 5 to case 6, D_I is reduced by about 3%, leading to a 20% increase in D_E. Furthermore, as turbulence decays within the inner ducts, the properties at the test-section centre depend on the nozzle-to-centre distance $D_N/2$. Tests with different D_N values are therefore performed to vary the turbulence characteristics.

2.3. *Turbulence properties in single-jet-array experiments*

Our previous studies employed the same jet generator in a turbulent wind tunnel (Mori *et al.* 2024; Watanabe *et al.* 2024, 2025). The tunnel had a 1 m-long test section with a square cross-section of 100×100 mm^2. A 6×6 array of jets was issued from one side of the test section, and their interaction generated nearly HIT decaying in the streamwise direction; the

Table 1: Experimental conditions and velocity statistics. Each case uses different test section geometries defined in figure 2. The distance from the nozzle exit to the test-section centre is $D_N/2$. The vector spacing in PIV is denoted by δ. The mean velocity gradient tensor is denoted by $A_{ij} = \partial\langle u_i\rangle/\partial x_j$. The rms fluctuations of u and v are denoted by u_{rms} and v_{rms}, respectively. The integral scales of u and v are denoted by L_u and L_v and are obtained by integrating the corresponding longitudinal autocorrelation functions. A dissipation scaling is used to provide an order-of-magnitude estimate of the turbulent kinetic-energy dissipation rate per unit mass, $\varepsilon = A\mathcal{U}^3/\mathcal{L}$ with $A = 1$, where $\mathcal{U}$ and $\mathcal{L}$ are the large-scale velocity and length scales. These are defined as $\mathcal{U} = \sqrt{2k_T/3}$ and $\mathcal{L} = (L_u + L_v + L_w)/3$, where $k_T = (u_{\mathrm{rms}}^2 + v_{\mathrm{rms}}^2 + w_{\mathrm{rms}}^2)/2$ is the turbulent kinetic energy. We assume $w_{\mathrm{rms}} = v_{\mathrm{rms}}$ and $L_w = L_v$ for the rms fluctuation and integral scale of w. The Taylor microscale and Kolmogorov scale are given by $\lambda = \sqrt{10(\mu/\rho)k_T/\varepsilon}$ and $\eta = (\mu/\rho)^{3/4}\varepsilon^{-1/4}$, respectively. The turbulent Reynolds number is $Re_\lambda = \rho\sqrt{2k_T/3}\lambda/\mu$. The table also includes ST_L, which is the mean strain rate $S = (|A_{xx}| + 2A_{yy} + 2A_{zz})/3$ with $A_{zz} = A_{yy}$ normalised by the time scale of large-scale motions, T_L. Most quantities are normalised by the jet velocity U_J and the jet spacing M. All statistics, except for $|A_{xx}|_{\max}$ and $(A_{yy})_{\max}$, are evaluated as ensemble and spatial averages within the measurement region. $|A_{xx}|_{\max}$ and $(A_{yy})_{\max}$ denote the maximum values of $|A_{xx}|$ and A_{yy}, respectively.

Case	1	2	3	4	5	6
D_I/M	35.4	34.6	33.8	26.9	26.0	25.2
D_N/M	77.5	77.5	77.5	60.4	60.4	60.4
D_E/M	6.7	8.3	10.0	6.7	8.3	10.0
$(D_N/2)/M$	38.75	38.75	38.75	30.2	30.2	30.2
δ/M	3.9×10^{-2}	5.2×10^{-2}	5.2×10^{-2}	4.0×10^{-2}	5.2×10^{-2}	5.2×10^{-2}
$\lvert A_{xx}\rvert_{\max}/(U_J/M)$	2.7×10^{-2}	2.7×10^{-2}	2.6×10^{-2}	3.3×10^{-2}	2.9×10^{-2}	2.8×10^{-2}
$\lvert A_{xx}\rvert/(U_J/M)$	2.0×10^{-2}	1.9×10^{-2}	1.8×10^{-2}	2.5×10^{-2}	2.1×10^{-2}	2.2×10^{-2}
$(A_{yy})_{\max}/(U_J/M)$	1.5×10^{-2}	1.4×10^{-2}	1.4×10^{-2}	1.7×10^{-2}	1.5×10^{-2}	1.5×10^{-2}
$(A_{yy})/(U_J/M)$	1.0×10^{-2}	1.0×10^{-2}	0.9×10^{-2}	1.3×10^{-2}	1.0×10^{-2}	1.1×10^{-2}
$(A_{yy})_{\max}/\lvert A_{xx}\rvert_{\max}$	0.54	0.52	0.53	0.53	0.50	0.54
$(A_{yy})/\lvert A_{xx}\rvert$	0.50	0.50	0.50	0.49	0.50	0.49
u_{rms}/U_J	4.1×10^{-2}	4.6×10^{-2}	4.8×10^{-2}	7.0×10^{-2}	6.9×10^{-2}	7.3×10^{-2}
v_{rms}/U_J	2.8×10^{-2}	3.1×10^{-2}	3.1×10^{-2}	4.4×10^{-2}	4.3×10^{-2}	4.4×10^{-2}
$u_{\mathrm{rms}}/v_{\mathrm{rms}}$	1.5	1.5	1.6	1.6	1.6	1.7
L_u/M	2.3	2.5	2.9	2.4	2.8	2.9
L_v/M	1.9	1.7	1.6	1.6	1.5	1.4
L_u/L_v	1.2	1.5	1.8	1.6	1.9	2.0
k_T/U_J^2	1.7×10^{3}	2.0×10^{3}	2.1×10^{3}	4.4×10^{3}	4.2×10^{3}	4.7×10^{3}
$\varepsilon/(U_J^3/M)$	1.8×10^{-5}	2.5×10^{-5}	2.6×10^{-5}	8.6×10^{-5}	7.7×10^{-5}	9.0×10^{-5}
λ/M	5.2×10^{-2}	4.9×10^{-2}	4.9×10^{-2}	3.9×10^{-2}	4.0×10^{-2}	4.0×10^{-2}
η/M	1.1×10^{-3}	1.0×10^{-3}	1.0×10^{-3}	0.74×10^{-3}	0.76×10^{-3}	0.74×10^{-3}
Re_λ	5.7×10^{2}	6.0×10^{2}	6.3×10^{2}	7.1×10^{2}	7.2×10^{2}	7.3×10^{2}
ST_L	1.2	1.0	1.0	0.84	0.76	0.76

turbulent flow exited through the open downstream end. The jet nozzles and the test-section cross-sectional geometry were identical to those used in the present experiments, and the operating conditions were also the same. Velocity measurements were conducted with the same PIV system as employed here. Results from these single-jet-array studies are cited

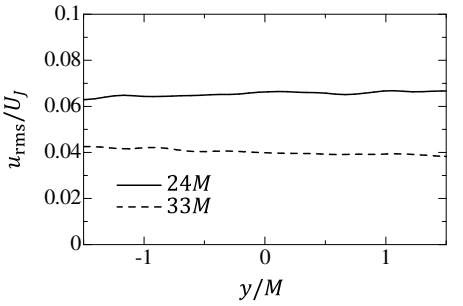

Figure 4: Vertical profiles of rms streamwise velocity fluctuations, $u_{\rm rms}$, at streamwise distances of $24M$ and $33M$ from the nozzles in the single jet-array configuration. The PIV velocity data are taken from Mori *et al.* (2024).

throughout this paper as a reference that approximates the initial turbulent state prior to the influence of mean strain for comparison with turbulence subject to axisymmetric expansion.

Figure 4 presents vertical profiles of the rms fluctuations of streamwise velocity u, $u_{\rm rms} = \sqrt{\langle u^2\rangle - \langle u\rangle^2}$, computed from the PIV data in Mori *et al.* (2024), where $\langle\ \rangle$ denotes ensemble averages of statistically independent samples. The profiles are shown at streamwise distances of $24M$ and $33M$ from the nozzles, slightly upstream of the inner-duct ends in the OMJA experiments. The results show that $u_{\rm rms}$ hardly depends on y, indicating that the velocity fluctuations are statistically homogeneous in the cross-sectional planes.

The turbulent Reynolds number is defined as $Re_\lambda = \rho\sqrt{2k_T/3}\lambda/\mu$, with the Taylor microscale $\lambda = \sqrt{10\mu k_T/(\rho\varepsilon)}$ and the turbulent kinetic energy k_T. In the turbulent wind tunnel with the single jet array, Re_λ is about 600 at $38M$ and about 730 at $30M$ downstream of the nozzle array. These locations approximately correspond to the distance from the nozzles to the test-section centre, $D_N/2$, in the OMJA experiments. The ratio of rms streamwise to vertical velocity fluctuations is about 1.08, close to values reported for grid turbulence (Krogstad & Davidson 2012; Kitamura *et al.* 2014; Isaza *et al.* 2014). Thus, the degree of isotropy is similar to that of grid turbulence, which has been used to investigate changes in initially nearly isotropic turbulence under axisymmetric contraction (Hussain & Ramjee 1976; Sjögren & Johansson 1998; Ayyalasomayajula & Warhaft 2006; Ertunç & Durst 2008; Alhareth *et al.* 2024).

2.4. *Particle image velocimetry*

Two-dimensional, two-component PIV is employed to investigate the turbulent flow field. Main measurements are conducted on the x–y plane at the centre of the test section ($z = 0$). For case 1, additional PIV measurements are conducted on the x–z plane at $y = 0$ and on the x–y plane at $z = 12$ mm to examine statistical axisymmetry. The setup, including components, seeding method and post-processing tools, is identical to that used in our previous studies on the single jet array (Mori *et al.* 2024; Watanabe *et al.* 2024). The PIV system consists of a double-pulse Nd:YAG laser (Dantec Dynamics, Dual Power 65-15), a high-speed camera (Dantec Dynamics, SpeedSense 9070) with 1280×800 pixel resolution equipped with a macro lens (Nikon, AI AF Micro Nikkor 105 mm F2.8D), and a synchroniser (Dantec Dynamics, 80N77) controlling the camera and laser via integrated software (Dantec Dynamics, DynamicStudio). The laser head, positioned beneath the test section, illuminates the x–y plane through a reflecting mirror. For the x–z plane measurements, an additional mirror is used to illuminate the plane with the laser sheet entering from the side wall. A lens unit attached to the laser head produces a laser sheet thinner than 1 mm, with a pulse width

under 4 ns. The camera, mounted on a tripod and mechanically isolated from the OMJA facility, views the illuminated plane. The field of view (FOV) is centred at $x = 0$, equidistant from the two jet arrays. The FOV size is approximately 100×60 mm^2 for cases 2, 3, 5 and 6, and 75×47 mm^2 for cases 1 and 4. These sizes are equivalent to $8.3M \times 5.0M$ and $6.3M \times 3.9M$, respectively. The smaller FOV in the latter cases results from obstruction by the test-section frame, as these involve a smaller inner-duct gap ($D_E < 100$ mm).

In line with previous studies of supersonic flows generated by Laval nozzles, the present PIV measurements employ condensed ethanol droplets as tracer particles (Clemens & Mungal 1991; Pizzaia & Rossmann 2018; Kouchi *et al.* 2019; Mori *et al.* 2024). In these studies, droplets are generated by fluid expansion in Laval nozzles, using air with evaporated ethanol or acetone as working fluid. Prior to each experiment, absorbent fabric soaked with approximately 100 mL of liquid ethanol is affixed to the inner wall of each plenum chamber using a 3D-printed stent. When the valves are opened, ethanol evaporates into the airflow through the plenum chambers, and the temperature drop in the Laval nozzles leads to condensation and droplet formation.

Condensation-generated tracers have very small diameters, making this seeding technique ideal for high-speed flows. Pizzaia & Rossmann (2018) and Kouchi *et al.* (2019) report ethanol/acetone droplet diameters of approximately 0.05–0.2 μm and 0.16 μm, respectively. In our facility, Rayleigh scattering is clearly observed, consistent with droplet diameters smaller than the visible-light wavelength (360–830 nm) (Mori *et al.* 2024). Based on these observations, we evaluate the Stokes number using a particle diameter $d_p = 0.2$ μm. The particle response time is $\tau_p = d_p^2 \rho_p / 18\mu = 9.69 \times 10^{-8}$ s, where $\rho_p = 789$ kg/m^3 is the ethanol density and $\mu = 1.81 \times 10^{-5}$ Pa·s is the viscosity of air. We evaluate the turbulence time scale at $26M$ downstream from the nozzles based on PIV data for turbulence generated by the single jet array (Mori *et al.* 2024). The shortest turbulence time scale is the Kolmogorov time scale, $\tau_\eta = (\mu/\rho\varepsilon)^{1/2} = 7.57 \times 10^{-6}$ s. The corresponding Stokes number is $St = \tau_p/\tau_\eta = 1.28 \times 10^{-2}$. Particles act as accurate tracers for $St < 0.1$ (Raffel *et al.* 2018), which is satisfied under the present experimental conditions.

Particle-image pairs are acquired at 15 Hz and processed in DynamicStudio using an adaptive PIV algorithm (Theunissen 2010) combined with universal outlier detection (Westerweel & Scarano 2005). The interrogation window sizes vary between 16×16 and 32×32 pixels, with a vector spacing of 8 pixels. This corresponds to 50% overlap for the minimum window and yields 159×99 velocity vectors per snapshot. The vector spacing, denoted by δ and normalised by the jet spacing S, is summarised in table 1. For the present setting, $\delta/M \approx 0.04$–0.05 is comparable to λ and about 40–70η, as estimated in § 3.4. Thus, the measurements do not resolve the smallest scales of motion but are sufficient to capture large-scale properties such as mean velocity and rms fluctuations. The interval between successive laser pulses is adjusted between 3 and 6 μs to maintain an average particle displacement of about 2–3 pixels across different cases, where the particle displacement refers to the distance of particle movements between two particle-images. This ensures that the average particle displacement is smaller than 1/4 of the interrogation window size and light-sheet thickness (Westerweel 1997). For the current PIV algorithm, the sub-pixel accuracy is expected to be of order 0.02–0.05 pixels (Raffel *et al.* 2018). With the present pixel size of about 0.08 mm and the pulse interval, this corresponds to about 1–3% of the rms velocity fluctuations. Under these settings for turbulence generated by a single jet-array, our previous studies successfully recovered the Batchelor-type decay law, the $-5/3$ law of energy spectra, the exponential tail of longitudinal autocorrelation functions, and the anomalous scaling of high-order moments of filtered velocity gradients (Mori *et al.* 2024;

Watanabe *et al.* 2024, 2025). These comparisons with turbulence theory, experiments and DNS validate the present PIV measurements.

Measurements are repeated 12–13 times per case to obtain more than 1000 velocity snapshots. The acquired velocity vectors are further processed to evaluate statistical quantities. The characteristic time scale of large-scale turbulent motions, defined as the ratio of the integral length scale to the rms velocity fluctuation (see § 3.4), is less than 0.002 s, which is much shorter than the sampling interval of 0.067 s. Velocity vectors from two consecutive particle-image pairs are therefore considered statistically independent. Statistics are evaluated using ensemble averages of all snapshots. For a variable f, its value in the nth snapshot is denoted by $f^{(n)}$. The ensemble average is given by

$$\langle f \rangle = \frac{1}{N_S} \sum_{n=1}^{N_S} f^{(n)}, \tag{2.1}$$

as a function of positions, where N_S is the total number of snapshots. Velocity components (u, v, w) are decomposed into mean and fluctuating parts, with fluctuations denoted by $u' = u - \langle u \rangle$, $v' = v - \langle v \rangle$ and $w' = w - \langle w \rangle$. The rms fluctuations are defined as $u_{\rm rms} = \langle u'^2 \rangle^{1/2}$, $v_{\rm rms} = \langle v'^2 \rangle^{1/2}$ and $w_{\rm rms} = \langle w'^2 \rangle^{1/2}$. Other velocity statistics are defined when they are introduced.

A spatial smoothing filter, implemented as a moving average, is applied to ensemble-averaged fields when presenting contour plots to highlight spatial distributions. Additionally, spatial averages within the FOV are used to describe bulk turbulence properties. Statistical uncertainties from finite sampling are estimated by dividing the dataset into two subsets; the rms differences between their statistics are shown as error bars in the results below.

2.5. *Temperature and pressure measurements*

In addition to PIV, supplemental experiments are conducted to measure temperature and static pressure at the centre of the test section to determine fluid properties required for evaluating the local Reynolds number and length scales. The methods follow those in our previous study using the same jet generator (Mori *et al.* 2024). Temperature is measured with a fine-sheathed K-type thermocouple (J Thermo, TJK-LS1501GP) of 0.15 mm sheath diameter, 100 mm length and a response time under 1 s. The thermocouple, supported by a stainless steel rod with thermal insulation, is inserted through closable holes in the top wall of the outer duct. The output voltage is processed and recorded by a data logger (Hioki, LR8431) with internal calibration at a sampling rate of 100 Hz. The mean temperature T is evaluated as the time average over 6 s and ensemble average of three runs. At the test-section centre, the mean temperature is approximately 290 ± 2 K under all conditions.

Static pressure is measured using the static port of an L-shaped standard Pitot tube (Testo, 0635 2145) connected to a pressure sensor (SMC, PSE543A). The analogue output of the sensor is recorded by an oscilloscope (Yokogawa, DL850E) at a sampling rate of 10 kHz. The Pitot tube is inserted from the top of the outer duct, in the same manner as the thermocouple. At the test-section centre, the mean gauge pressure is approximately 10^2 PaG, much smaller than atmospheric pressure.

Based on the measured mean temperature T and pressure P, the density ρ is evaluated from the equation of state, $P = \rho R T$, with the gas constant $R = 287$ J/(kg·K). The viscosity μ is determined using Sutherland's law,

$$\mu = \mu_0 \left(\frac{T}{T_0} \right)^{3/2} \frac{T_0 + S_\mu}{T + S_\mu}, \tag{2.2}$$

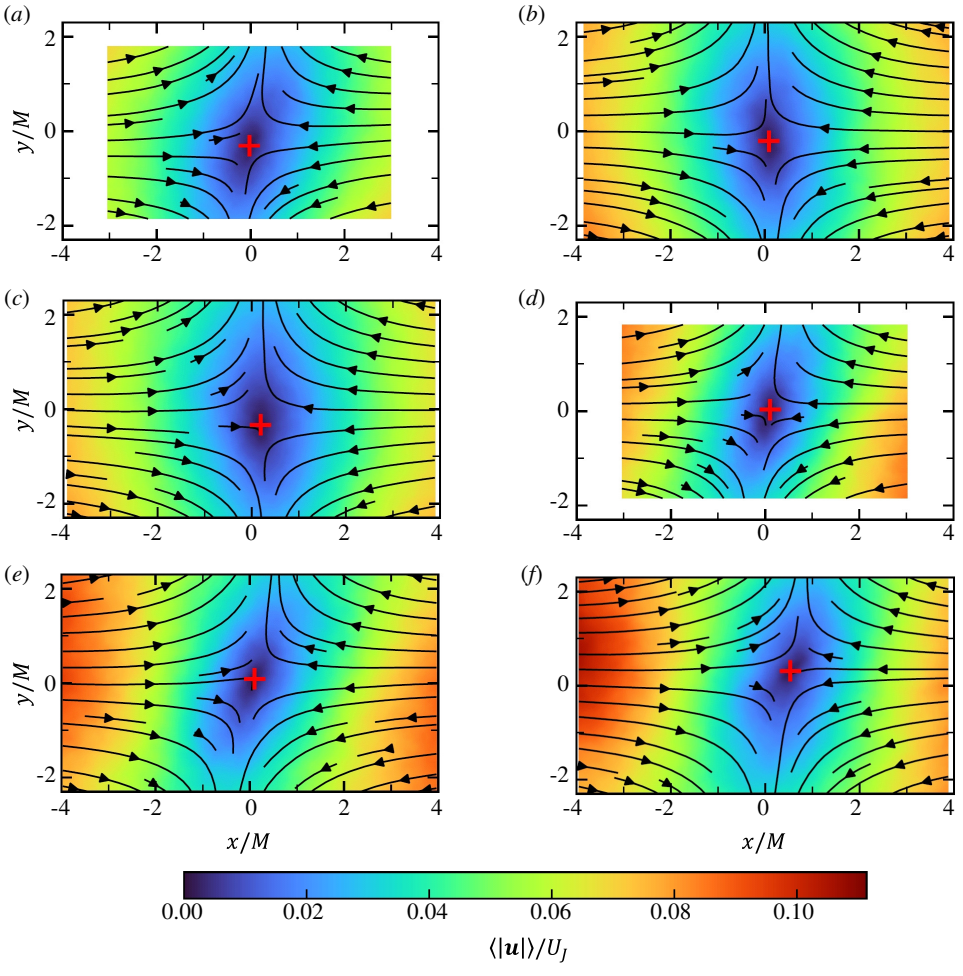

Figure 5: Averaged velocity fields coloured by the mean velocity magnitude, $|\langle \boldsymbol{u} \rangle| = \sqrt{\langle u \rangle^2 + \langle v \rangle^2}$, on the x–y plane at $z = 0$. Black lines with arrows indicate streamlines. Red crosses denote the minimum value of $|\langle \boldsymbol{u} \rangle|$. Panels show results for different test section geometries: (*a*) case 1, (*b*) case 2, (*c*) case 3, (*d*) case 4, (*e*) case 5 and (*f*) case 6.

where $T_0 = 273$ K is the reference temperature, $S_\mu = 110.4$ K is the Sutherland constant and $\mu_0 = 1.724 \times 10^{-5}$ Pa·s is the reference viscosity.

Pressure and temperature measurements at the test-section centre yield density $\rho = 1.25$ kg/m^3, viscosity $\mu = 1.81 \times 10^{-5}$ Pa·s and kinematic viscosity $\nu = \mu/\rho = 1.44 \times 10^{-5}$ m^2/s. These values do not vary among the different test-section geometries.

3. Results and discussion

3.1. *Mean flow field*

Figure 5 presents the mean flow field for each case, showing mean velocity streamlines and a colour contour of the magnitude of the mean velocity vector, $|\langle \boldsymbol{u} \rangle|$. The streamlines indicate that opposing flows approach from both sides along the x-direction and expand

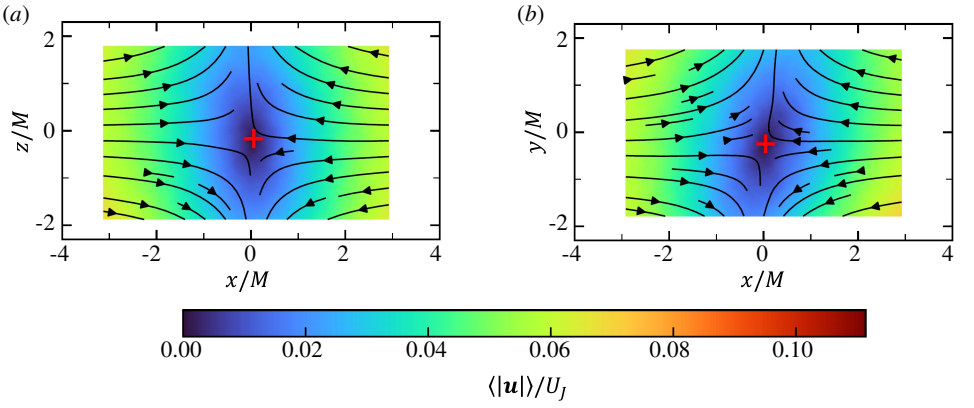

Figure 6: Averaged velocity fields coloured by the mean velocity magnitude in case 1: (*a*) $|\langle \boldsymbol{u} \rangle| = \sqrt{\langle u \rangle^2 + \langle w \rangle^2}$ on the x–z plane at $y = 0$; (*b*) $|\langle \boldsymbol{u} \rangle| = \sqrt{\langle u \rangle^2 + \langle v \rangle^2}$ on the x–y plane at $z/M = 1$. Black lines with arrows indicate streamlines. Red crosses denote the minimum value of $|\langle \boldsymbol{u} \rangle|$.

vertically near the test-section centre. The stagnation point is identified by the minimum value of $|\langle \boldsymbol{u} \rangle|$, close to zero, and is marked by red crosses. In all cases, the stagnation point is located near the geometric centre of the test section, $(x, y) = (0, 0)$, owing to the symmetric configuration of the test section and jet arrays. The streamline patterns imply $\partial\langle u \rangle/\partial x < 0$ and $\partial\langle v \rangle/\partial y > 0$, consistent with axisymmetric expansion described by (1.3). The mean velocity remains below 45 m/s in all cases, implying that the mean flow Mach number is less than 0.3.

Figure 6 visualises the mean flow on the x–z plane at $y = 0$ and on the x–y plane at $z/M = 1$. Owing to the geometry of the test section and jet arrays, the x–z plane at $y = 0$ is equivalent to the x–y plane at $z = 0$. The mean velocity pattern of axisymmetric expansion is visible on the x–z plane as well as on the off-centre x–y plane.

The mean velocity gradients associated with axisymmetric strain are given by the diagonal components of $\boldsymbol{A}$ in (1.1), namely $A_{xx} = \partial\langle u \rangle/\partial x$, $A_{yy} = \partial\langle v \rangle/\partial y$ and $A_{zz} = \partial\langle w \rangle/\partial z$. Since central-difference approximations introduce significant errors due to statistical uncertainty in the mean velocity distribution, the gradients are instead obtained by fitting $\langle u \rangle$, $\langle v \rangle$ and $\langle w \rangle$ with bicubic functions (x, y) or (x, z). This choice is motivated by the observation that a third-order polynomial adequately captures one-dimensional profiles of mean velocities along either x, y or z axis. Higher-order functions were also tested but offered no improvement in accuracy and instead introduced unnecessary complexity and the risk of over-fitting.

Figures 7 and 8 show colour contours of $|A_{xx}|$ and A_{yy}, normalised by their respective maxima $|A_{xx}|_{\max}$ and $(A_{yy})_{\max}$. In all cases, $|A_{xx}|$ and A_{yy} decrease with increasing $|x|$, indicating that the mean strain strengthens as the flow enters the gap between the inner ducts and approaches the test-section centre. At $x \approx 0$, both $|A_{xx}|$ and A_{yy} increase with $|y|$ in cases 1–3, but the dependence on x is stronger than on y.

Table 1 includes the maximum values of $|A_{xx}|$ in each case. The mean velocity in the x direction decreases from that in the inner duct to nearly zero at the stagnation point, and when D_E is large this decrease occurs over a longer distance. Consequently, the mean velocity gradient tends to be smaller for larger D_E. For fixed D_N, $|A_{xx}|_{\max}$ decreases with increasing D_E, but variations in D_N also affect $|A_{xx}|_{\max}$, indicating that it is not determined solely by D_E.

A key feature of axisymmetric expansion is the ratio of the diagonal velocity gradients,

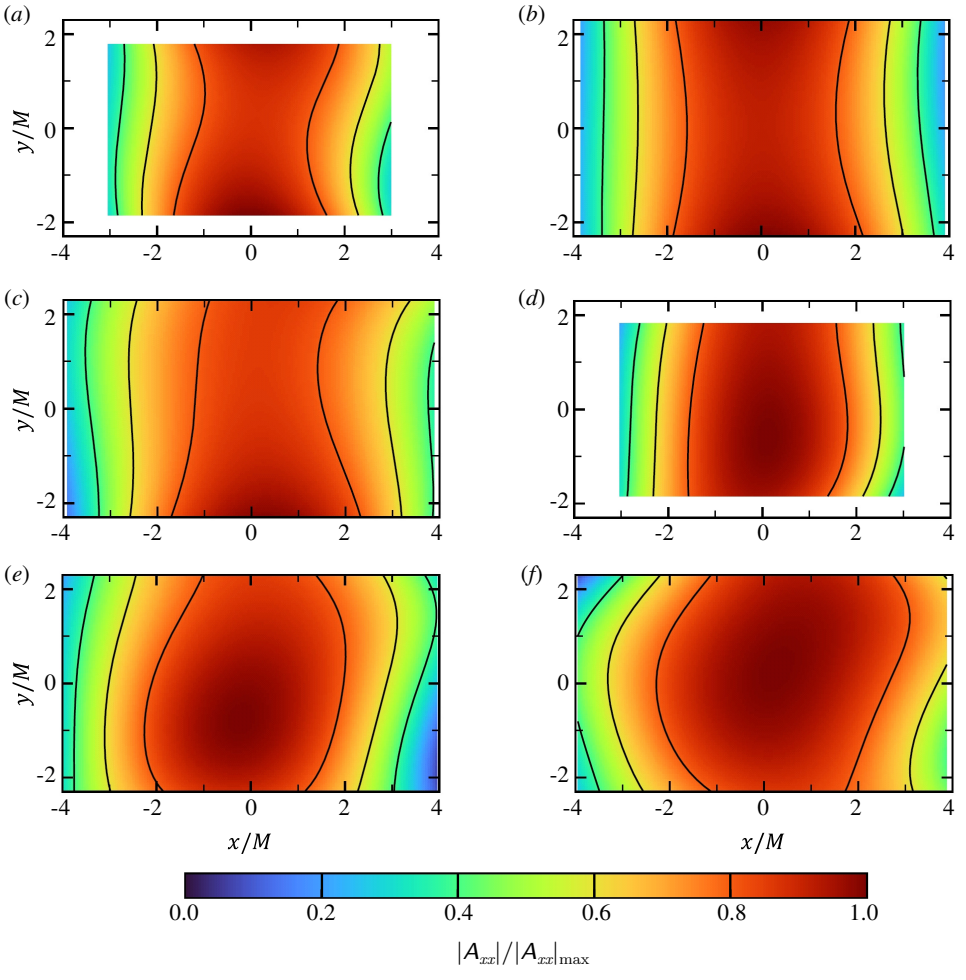

Figure 7: Distributions of the mean velocity gradient magnitude $|A_{xx}|$ normalised by its maximum value $|A_{xx}|_{\max}$. Panels show results for different test section geometries: (*a*) case 1, (*b*) case 2, (*c*) case 3, (*d*) case 4, (*e*) case 5 and (*f*) case 6.

satisfying $A_{yy} = A_{zz} = -A_{xx}/2 > 0$. Figure 9 shows the distribution of $-A_{yy}/A_{xx}$ on the x–y plane at $z = 0$. Deviations from $-A_{yy}/A_{xx} = 0.5$ are observed only near the edges of the measurement region. In most regions close to the test-section centre, $-A_{yy}/A_{xx}$ is close to 0.5, lying within the range 0.4–0.6. Figure 10(*a*) presents the distribution of $-A_{zz}/A_{xx}$ measured on the x–z plane at $y = 0$ in case 1. As with $-A_{yy}/A_{xx}$, $-A_{zz}/A_{xx}$ is close to 0.5 except near the edges of the measurement region. Taken together, $-A_{yy}/A_{xx} \approx -A_{zz}/A_{xx} \approx 0.5$ provides direct evidence of the formation of axisymmetric expansion and suggests that the continuity equation for the mean velocity in an incompressible flow is satisfied without compressibility effects. This is also consistent with the subsonic mean velocity, as low as about 45 m/s. Figure 10(*b*) shows the distribution of $-A_{yy}/A_{xx}$ on the x–y plane at $z/M = 1$ in case 1. Even on this off-centre plane, $-A_{yy}/A_{xx} \approx 0.5$ holds except near the edges of the measurement region. These results demonstrate that axisymmetric strain is broadly established in the gap between the inner ducts of the two jet generators.

Table 1 lists the maximum values of $|A_{xx}|$ and A_{yy}, denoted by $|A_{xx}|_{\max}$ and $(A_{yy})_{\max}$,

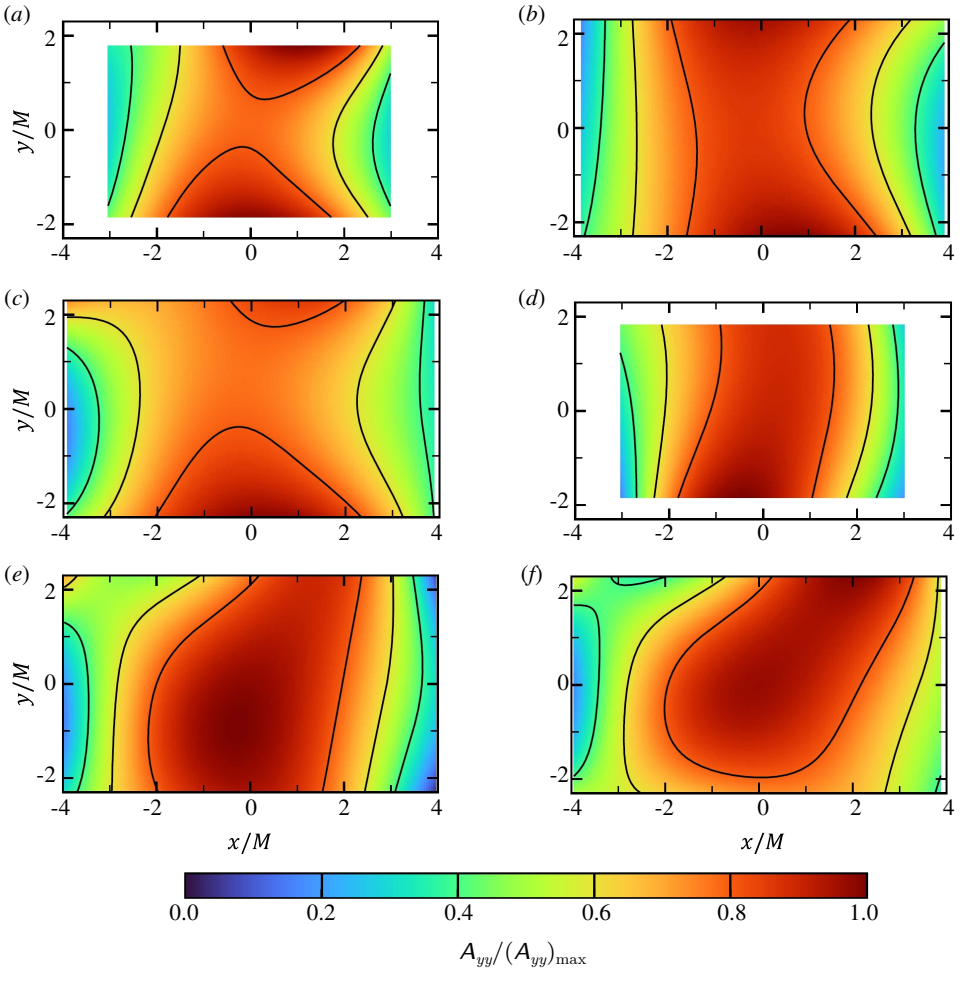

Figure 8: Same as figure 7, but for A_{yy} normalised by $(A_{yy})_{\max}$: (*a*) case 1, (*b*) case 2, (*c*) case 3, (*d*) case 4, (*e*) case 5 and (*f*) case 6.

together with spatially averaged values of $|A_{xx}|$ and A_{yy}. The ratios $(A_{yy})_{\max}/|A_{xx}|_{\max}$ and $A_{yy}/|A_{xx}|$ are also shown, both close to 1/2. Using the incompressible continuity equation, A_{zz} is estimated as $A_{zz} = -A_{xx} - A_{yy}$, which yields $A_{yy} \approx A_{zz}$ when $A_{yy} \approx -A_{xx}/2$. Thus, the condition for axisymmetric expansion is satisfied for both maximum and average values. Moreover, the relation $A_{yy} \approx A_{zz}$ indicates that the flow is statistically axisymmetric in the y and z directions.

In summary, all cases successfully produce a mean strain characterised by compression in the x direction and expansion in the y and z directions. Axisymmetric expansion, with $A_{xx} : A_{yy} : A_{zz} = -2 : 1 : 1$, is broadly observed near the test-section centre. This condition is uniformly satisfied for $|x/M| \leqslant 3$ and $|y/M| \leqslant 1.5$. Although $-A_{yy}/A_{xx}$ remains approximately constant, both $-A_{xx}$ and A_{yy} exhibit spatial variations, such that the strain rate intensifies as the flow approaches the test-section centre in the x direction. Similar non-uniformity of axisymmetric strain has often been reported in wind-tunnel experiments with variable cross-sections (Ayyalasomayajula & Warhaft 2006). The relation $A_{yy} = A_{zz}$, implied by the continuity equation, indicates statistical axisymmetry in the y and z directions,

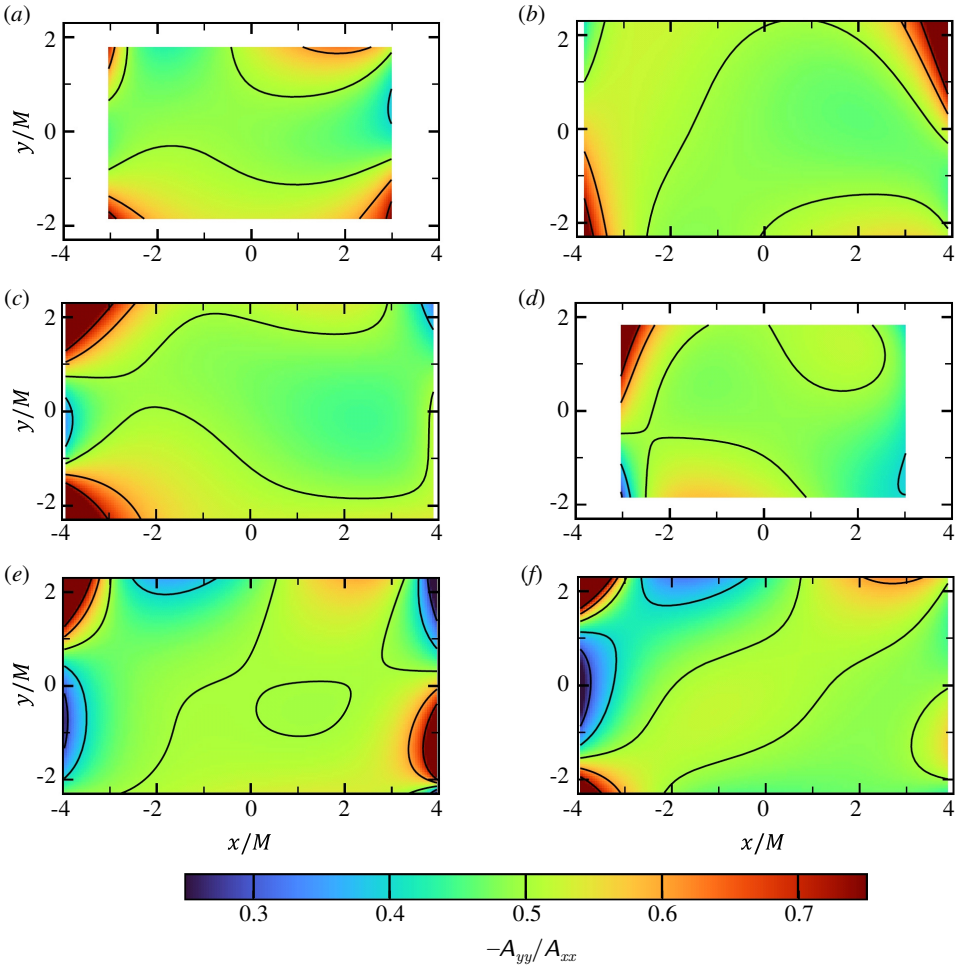

Figure 9: Distributions of the ratio of mean velocity gradients, $-A_{yy}/A_{xx}$. Panels show results for different test section geometries: (*a*) case 1, (*b*) case 2, (*c*) case 3, (*d*) case 4, (*e*) case 5 and (*f*) case 6.

consistent with the symmetry of the test section and jet generators. Importantly, $-A_{xx}/2 = A_{yy} = A_{zz}$ is satisfied not only along the symmetry axis ($y = 0$) but also for $y \neq 0$ and $z \neq 0$, demonstrating that the mean strain remains axisymmetric throughout the central region of the test section. This mean strain characterisation provides the basis for interpreting the turbulence statistics discussed below.

3.2. *One-point statistics of velocity fluctuations*

One-point statistics of velocity fluctuations are evaluated to characterise the turbulence properties under axisymmetric expansion. Table 1 reports the spatially averaged values of u_{rms} and v_{rms} for all cases. Cases 1–3 exhibit lower values of u_{rms} and v_{rms} than cases 4–6. The turbulence generated by jet interaction decays within the inner duct. Since cases 1–3 employ longer inner ducts, the turbulence decays more before reaching the test-section centre, leading to smaller rms velocity fluctuations in the region where the mean strain forms. The present experiments test three values of the distance D_E between the ends of the two inner

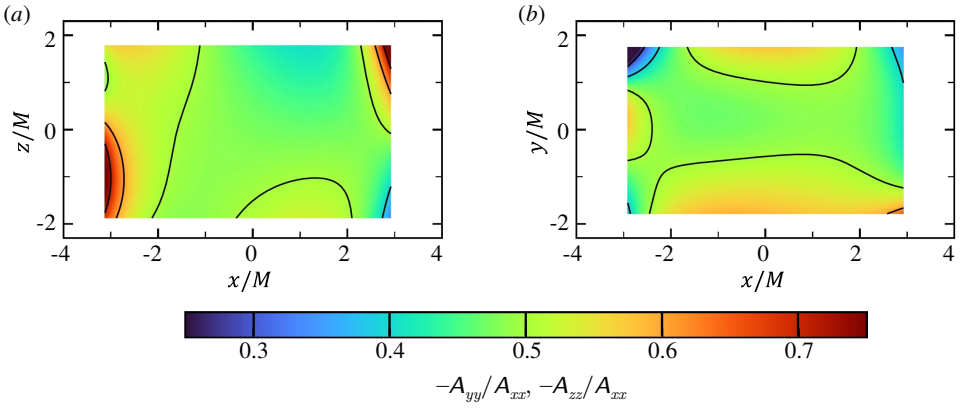

Figure 10: Distributions of (*a*) $-A_{zz}/A_{xx}$ on the x–z plane at $y = 0$ and (*b*) $-A_{yy}/A_{xx}$ on the x–y plane at $z/M = 1$ in case 1.

ducts. However, the rms velocity fluctuations are less sensitive to D_E than to D_N. In all cases, $u_{\rm rms}$ exceeds $v_{\rm rms}$, indicating anisotropy. Turbulence generated by the single jet array exhibits $u_{\rm rms}/v_{\rm rms} \approx 1.08$ (Mori *et al.* 2024). In the present experiments, the nearly HIT generated by jet interaction experiences axisymmetric expansion near the test-section centre, resulting in anisotropic velocity fluctuations. Table 1 also includes $u_{\rm rms}/v_{\rm rms}$ values evaluated from spatial averages of $u_{\rm rms}$ and $v_{\rm rms}$. This ratio exceeds 1.4, much larger than the value of 1.08 for turbulence without axisymmetric expansion. DNSs of initially isotropic turbulence subject to axisymmetric expansion have also shown that $u_{\rm rms}/v_{\rm rms} > 1$ (Lee 1989), even though the turbulent Reynolds number, estimated in § 3.4, is much larger in the present experiments. Thus, the observed increase in $u_{\rm rms}/v_{\rm rms}$ due to axisymmetric expansion is consistent with previous numerical results.

Figures 11 and 12 show the distributions of $u_{\rm rms}$ and $v_{\rm rms}$ on the x–y plane at $z = 0$. The colour contours indicate relative deviations from the spatially averaged value in the FOV, $F_{\rm avg}$, defined as $\Delta(F) = (F - F_{\rm avg})/F_{\rm avg}$ for $F = u_{\rm rms}$ or $v_{\rm rms}$. In figure 11, $u_{\rm rms}$ increases toward $x = 0$ from both sides, whereas $v_{\rm rms}$ shows little dependence on x for cases 1–3 and decreases to the centre for cases 4–6. Turbulence begins to be influenced by the mean strain near the ends of the inner ducts. As it is advected by the mean flow toward the test-section centre, it is exposed to the mean strain for a longer time. Additionally, the mean strain intensifies toward the test-section centre. This combination of strain intensification and accumulation of strain effects likely contributes to the increase in $u_{\rm rms}$ near the test-section centre. In contrast, variations in $v_{\rm rms}$ in the same region are less pronounced. DNS studies of turbulence subject to axisymmetric strain at low Reynolds numbers have shown that the strain exerts stronger influence on rms velocity fluctuations in the symmetry axis direction, here the x direction, than in the lateral (y and z) directions (Lee 1989). These numerical findings qualitatively agree with the greater changes in $u_{\rm rms}$ observed toward the test-section centre.

Under axisymmetric expansion with $A_{xx} = -2A_{yy} = -2A_{zz} < 0$, the production term of turbulent kinetic energy of the α-directional velocity component is written as $P_\alpha = -\langle u_\alpha'^2 \rangle A_{\alpha\alpha}$ with $\alpha = x, y$ or z, where no summation is applied over α (Nieuwstadt & Boersma 2016). This gives $P_x > 0$ and $P_y = P_z < 0$, indicating an increase in the streamwise and a decrease in the transverse velocity fluctuations. Moreover, when turbulence is initially isotropic with $\langle u'^2 \rangle = \langle v'^2 \rangle = \langle w'^2 \rangle$, the relation $A_{xx} : A_{yy} : A_{zz} = -2 : 1 : 1$ yields $P_x = 2|P_y| = 2|P_z|$, implying that the strain induces greater changes to the velocity fluctuations in the x direction than in the transverse (y and z) directions. Consistently, a significant increase

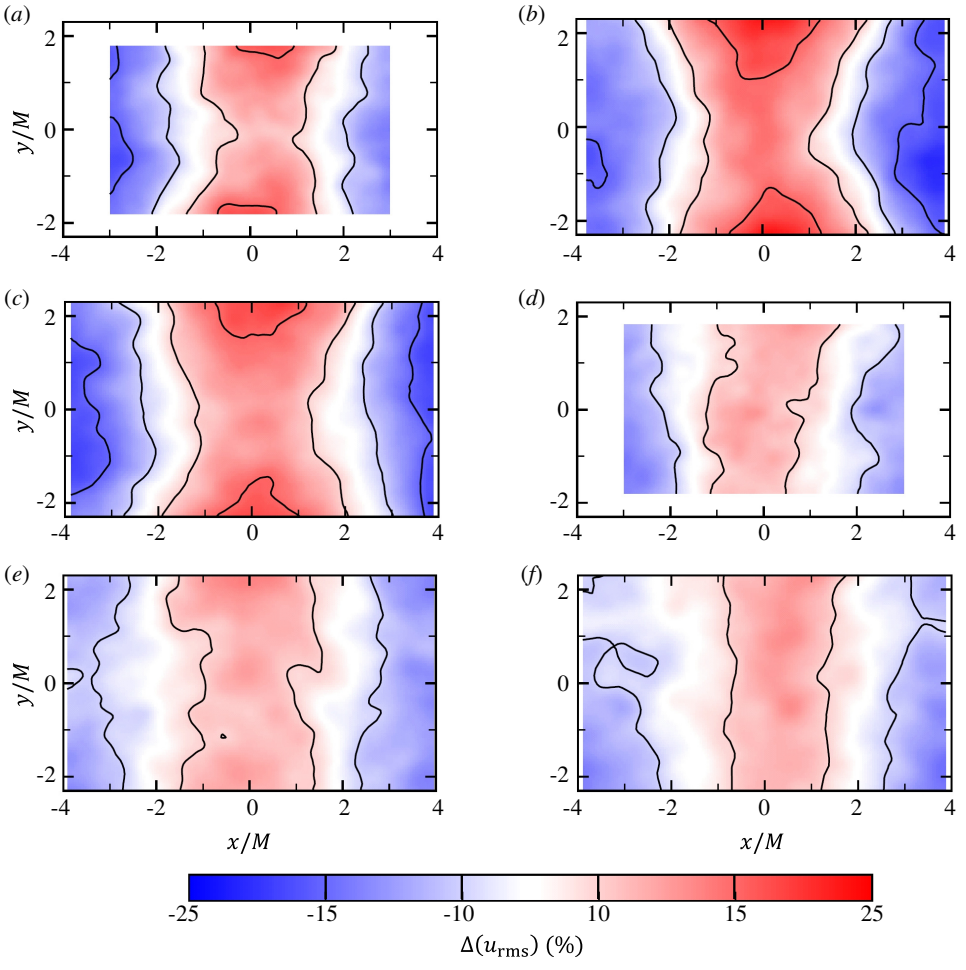

Figure 11: Relative difference of rms velocity fluctuations in the x direction, $u_{\rm rms}$, from the spatially averaged value $(u_{\rm rms})_{\rm avg}$, defined as $\Delta(u_{\rm rms}) = [u_{\rm rms} - (u_{\rm rms})_{\rm avg}]/(u_{\rm rms})_{\rm avg}$, on the x–y plane at $z = 0$. Here the subscript "avg" denotes spatial averages within the FOV. Panels show results for different test section geometries: (a) case 1, (b) case 2, (c) case 3, (d) case 4, (e) case 5 and (f) case 6.

in $u_{\rm rms}$ toward the test-section centre is observed in figure 11. These explanations are also consistent with DNS and RDT results (Lee 1989). For axisymmetric contraction, the signs of P_α are reversed; transverse velocity fluctuations are amplified and longitudinal fluctuations attenuated, resulting in a decrease in $u_{\rm rms}/v_{\rm rms}$ (Lee 1989; Ayyalasomayajula & Warhaft 2006).

Figure 13 compares $v_{\rm rms}$ and $w_{\rm rms}$ along the x direction at the test-section centre, $(y, z) = (0, 0)$, for case 1. These components exhibit similar rms levels, as indicated by $v_{\rm rms}/w_{\rm rms} \approx 1$, which is required for statistical axisymmetry. This also follows from the geometry of the test section and jet arrays, which are identical in the y and z directions.

Statistical axisymmetry in the present set-up requires that, at a given x, velocity statistics depend solely on $r_{yz} = \sqrt{y^2 + z^2}$ and are independent of the azimuthal angle $\theta = \tan^{-1}(y/z)$. Table 2 compares $u_{\rm rms}$ at the same r_{yz} but at different (y, z) locations at $x = 0$ on three

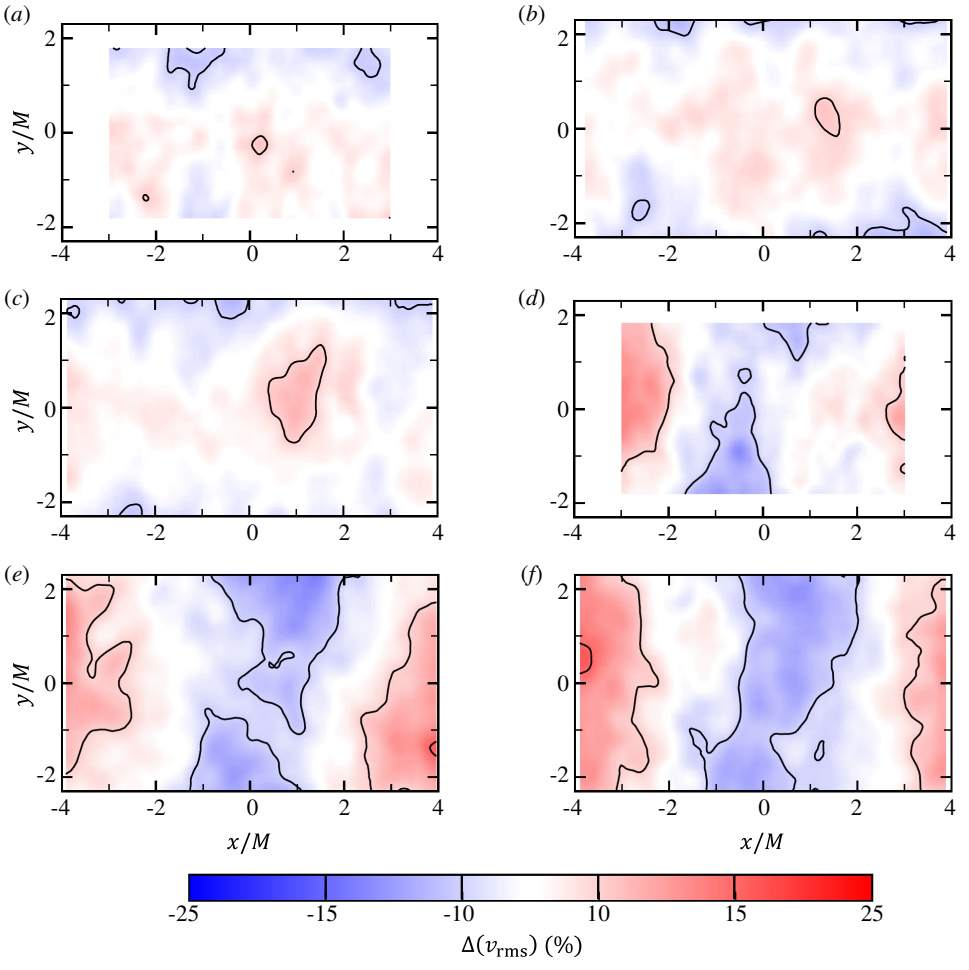

Figure 12: Same as figure 11, but for rms velocity fluctuations in the y direction, v_{rms}: (a) case 1, (b) case 2, (c) case 3, (d) case 4, (e) case 5 and (f) case 6. The relative difference is defined as $\Delta(v_{\mathrm{rms}}) = [v_{\mathrm{rms}} - (v_{\mathrm{rms}})_{\mathrm{avg}}]/(v_{\mathrm{rms}})_{\mathrm{avg}}$.

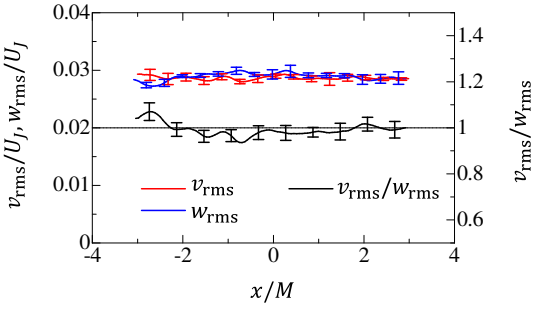

Figure 13: x-directional distributions of rms velocity fluctuations in the y and z directions, v_{rms} and w_{rms}, and their ratio $v_{\mathrm{rms}}/w_{\mathrm{rms}}$ at $(y, z) = (0, 0)$ in case 1.

Table 2: Radial variations of u_{rms} at different azimuthal locations at $x = 0$ in case 1.

y/M	z/M	r_{yz}/M	u_{rms}/U_J
1.0	0.0	1.0	0.046
0.0	1.0	1.0	0.047
1.1	0.0	1.1	0.046
0.0	1.1	1.1	0.048
0.4	1.0	1.1	0.048
1.4	0.0	1.4	0.046
0.0	1.4	1.4	0.048
1.0	1.0	1.4	0.047

measurement planes: the x–y planes at $z/M = 0$ and 1, and the x–z plane at $y = 0$. For $r_{yz}/M = 1$, two points are presented because the locations at this r_{yz} on the x–y plane at $z/M = 1$ and the x–z plane at $y = 0$ are identical. Although the square cross-section and square nozzle arrangement could, in principle, introduce θ-dependence, u_{rms} at the same r_{yz} shows no significant variation across (y, z) locations. Therefore, the square geometries do not introduce θ-dependence near the test-section centre.

Large-scale anisotropy is often characterised using the normalised anisotropy tensor of Reynolds stress (Pope 2000), defined as

$$b_{ij} = \frac{\langle u_i' u_j' \rangle}{\langle u_k' u_k' \rangle} - \frac{1}{3}\delta_{ij}, \tag{3.1}$$

where the summation convention is applied to repeated indices, $i, j, k = x, y$ or z, and δ_{ij} is the Kronecker delta. Second and third invariants of b_{ij}, denoted by B_2 and B_3, are given by $B_2 = (b_{ij}b_{ji}/6)^{1/2}$ and $B_3 = (b_{ij}b_{jk}b_{ki}/6)^{1/3}$. Anisotropy states are commonly visualised using a plot of (B_2, B_3), known as the Lumley triangle. The PIV measurements of (u, v) on the x–y plane provide b_{xx}, b_{yy} and $b_{xy} = b_{yx}$. Based on the assumption of axisymmetry at $(y, z) = (0, 0)$, the following conditions are adopted in the analysis of B_2 and B_3: $b_{yy} = b_{zz}$ and $b_{ij} = 0$ for $i \neq j$. The present PIV yields $|\langle u'v' \rangle|/u_{\mathrm{rms}}v_{\mathrm{rms}} < 0.1$ at $(y, z) = (0, 0)$ for all cases, indicating that b_{ij} with $i \neq j$ is sufficiently small. These simplifications for axisymmetric expansion yield $B_2 = B_3$. Accordingly, this study examines the spatial distribution of B_2. The omission of b_{12} and b_{21} has negligible effect, as their inclusion hardly alters B_2 values. For isotropic turbulence, $B_2 = 0$. As the flow departs from isotropy under axisymmetric expansion, $B_2 = B_3$ increases, with the theoretical upper bound of 1/3 attained when $\langle u'^2 \rangle \gg \langle v'^2 \rangle = \langle w'^2 \rangle$.

Figure 14 shows the x-directional distribution of B_2 at $(y, z) = (0, 0)$. Nearly HIT generated by the single jet array exhibits $B_2 \approx 0.03$ (Mori *et al.* 2024). In contrast, the present experimental setup yields higher B_2 values, indicating that the flow becomes anisotropic. For all cases, B_2 increases from both sides toward the test-section centre, demonstrating that anisotropy intensifies as the fluid subjected to the mean strain is advected with the mean flow. This increasing trend of B_2 is observed consistently across all test section geometries.

Figure 15 presents the profiles of skewness and flatness of u, defined as $S_u = \langle u'^3 \rangle / \langle u'^2 \rangle^{3/2}$ and $F_u = \langle u'^4 \rangle / \langle u'^2 \rangle^2$. For Gaussian velocity fluctuations, $S_u = 0$ and $F_u = 3$. Deviations

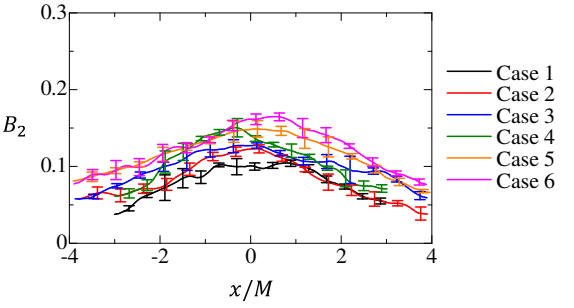

Figure 14: x-directional distribution of the invariant B_2 of the normalized anisotropy tensor b_{ij} along the centreline, $(y, z) = (0, 0)$.

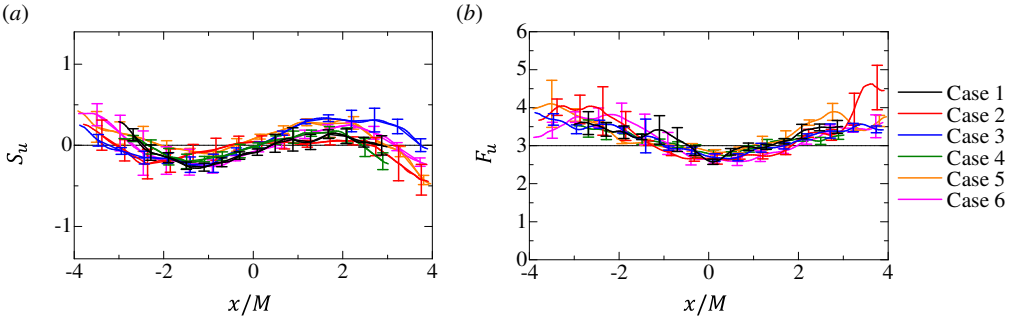

Figure 15: Distributions of (a) skewness S_u and (b) flatness F_u of x-directional velocity fluctuations along the centreline, $(y, z) = (0, 0)$.

from these values typically indicate large-scale intermittency, i.e. intermittency of energy-containing motions (Veeravalli & Warhaft 1989; Davidson 2015). This differs from small-scale intermittency, which refers to the burstiness of small-scale motions, typically evident in velocity-gradient statistics. Large-scale intermittency is observed in turbulent free shear flows (e.g. jets and wakes) and other inhomogeneous turbulent flows, where the presence and absence of large coherent structures alternate at a fixed point. In such cases, the magnitudes of skewness and flatness can reach values as large as 1 and 5, respectively (Kang & Meneveau 2008; Matsushima *et al.* 2021; Nakamura *et al.* 2022, 2023). In the present measurements, $|S_u|$ remains below 0.3 and F_u is close to 3 near the test-section centre, showing that large-scale intermittency is negligible in this region. While F_u tends to exceed 3 as $|x|$ increases, suggesting slight intermittency in the flow entering the gap region from the inner duct ends, the deviation remains moderate and far smaller than that in flows with pronounced large-scale intermittency.

3.3. *Two-point statistics and energy spectra*

We examine two-point statistics and energy spectra from PIV on the x–y plane at $z = 0$ to evaluate integral length scales and the scale dependence of velocity fluctuations, using autocorrelation functions, energy spectra and structure functions. For evaluating these quantities, spatial averages in the x and y directions are taken over $|x| < 2M$ and $|y| < M$, respectively, thereby excluding corner regions where the mean velocity gradients depart from axisymmetric strain.

Large-scale properties are examined using the longitudinal autocorrelation functions of

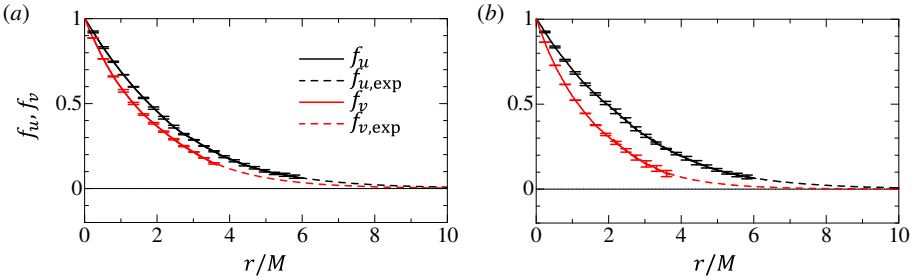

Figure 16: Longitudinal autocorrelation functions of u and v, denoted by f_u and f_v, respectively, for (a) case 1 and (b) case 4. Dashed-dotted lines indicate exponential fits that approximate the correlations at large separation distances.

velocity fluctuations at two points separated by a distance r, defined as

$$f_u(r,x,y) = \frac{\langle u'(x-r/2,y)u'(x+r/2,y)\rangle}{\langle u'^2(x,y)\rangle}, \tag{3.2}$$

$$f_v(r,x,y) = \frac{\langle v'(x,y-r/2)v'(x,y+r/2)\rangle}{\langle v'^2(x,y)\rangle}. \tag{3.3}$$

These functions are used to estimate the integral length scale, which characterises large-scale motions. The symmetric forms of the autocorrelation functions, i.e. correlations between $x+r/2$ and $x-r/2$ rather than between x and $x+r$, are used to evaluate turbulent properties at a given point because the flow is statistically inhomogeneous. Here, f_u is evaluated at $x=0$ and f_v at $y=0$ with spatial averaging applied in the y and x directions, respectively.

Figure 16 presents f_u and f_v for cases 1 and 4, representing $D_N = 930$ mm and 725 mm. Both f_u and f_v decrease from unity as r increases, indicating decorrelation of velocity fluctuations between two spatially separated points. The measurable range of r is limited by the PIV FOV, and although f_u and f_v are expected to decay to zero, this decay cannot be fully captured. It is known that the tails of autocorrelation functions at large r are well approximated by an exponential form $a_f \exp(-b_f r)$ (Morikawa *et al.* 2008; Bewley *et al.* 2012; Griffin *et al.* 2019; Mori *et al.* 2024). For the measured r range where f_u and f_v fall below 0.3, a least-squares method is used to determine a_f and b_f. The resulting fits, $f_{u,\mathrm{exp}}$ and $f_{v,\mathrm{exp}}$, are also shown in figure 16, confirming that the exponential function accurately approximates the measured autocorrelation of both u and v.

The integral scales are computed by integrating the autocorrelation functions with respect to r, defined as $L_u = \int f_u(r)\,dr$ and $L_v = \int f_v(r)\,dr$. The integration is performed from $r = 0$ to the position where the correlation function becomes zero. Since the PIV measurements do not always capture correlations at large r, the integral scales are estimated with the aid of the exponential approximations $f_{u,\mathrm{exp}}$ and $f_{v,\mathrm{exp}}$, following previous studies (Morikawa *et al.* 2008; Bewley *et al.* 2012; Griffin *et al.* 2019; Mori *et al.* 2024):

$$L_u = \int_0^{r_1} f_u(r)\,dr + \int_{r_1}^{r_2} f_{u,\mathrm{exp}}(r)\,dr, \tag{3.4}$$

where r_1 is defined by the condition $f_u(r_1) = 0.3$, and r_2 is the position at which $f_{u,\mathrm{exp}}(r)$ reaches 1×10^{-5}. The integral scale in the y direction, L_v, is computed in the same manner using f_v and $f_{v,\mathrm{exp}}$ as in (3.4). Table 1 lists L_u, L_v and their ratio L_u/L_v for each case. Nearly HIT generated by the single jet array yields $L_u/L_v \approx 1.03$ (Mori *et al.* 2024). In contrast, turbulence subject to axisymmetric expansion in the present experiments exhibits larger values of L_u/L_v, indicating increased anisotropy. For the single jet array case, both

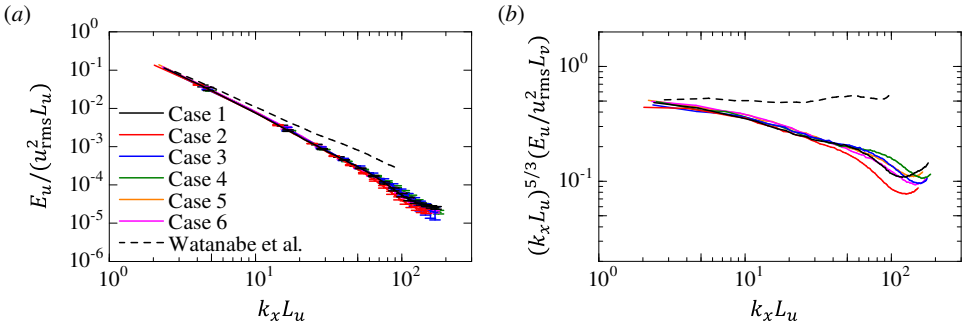

Figure 17: (*a*) Longitudinal energy spectra of x-directional velocity fluctuations, $E_u(k_x)$, where k_x is the x-directional wavenumber. (*b*) Compensated spectra $k_x^{5/3}E_u$. Results for nearly HIT generated by the single jet array, evaluated 605 mm downstream of the nozzles, are shown for comparison (Watanabe *et al.* 2025).

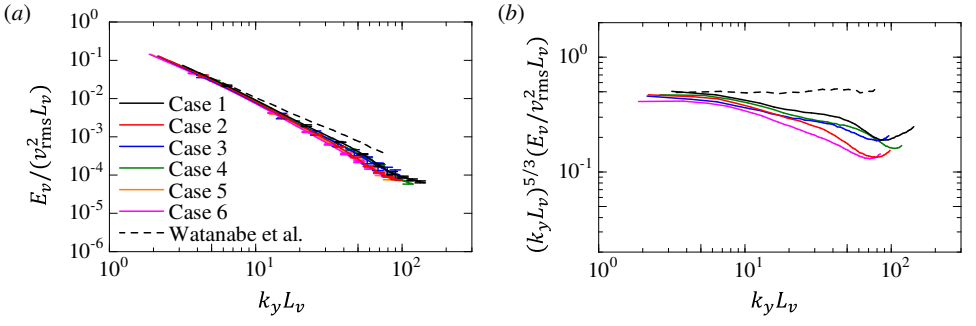

Figure 18: (*a*) Longitudinal energy spectra of y-directional velocity fluctuations, $E_v(k_y)$, where k_y is the y-directional wavenumber. (*b*) Compensated spectra $k_y^{5/3}E_v$. Results for nearly HIT generated by the single jet array, evaluated 605 mm downstream of the nozzles, are shown for comparison (Watanabe *et al.* 2025).

L_u and L_v are about 0.022 m in the measurement region, comparable to the present setup. Relative to this reference, L_u increases and L_v tends to decrease in the current experiments, with the deviations from the reference being more pronounced for L_u than for L_v. Although the single jet array case does not provide exact turbulence statistics prior to the onset of mean strain in the OMJA experiments, it is noteworthy that the greater changes observed in L_u are consistent with DNS results at low Reynolds numbers of Lee (1989), where L_u departs more strongly from the isotropic state than L_v under axisymmetric expansion. The increase in L_u and the decrease in L_v under axisymmetric expansion are also predicted by RDT, which attributes these trends to anisotropic redistribution of energy in three-dimensional wavenumber space and the consequent changes in the one-dimensional spectra (Lee 1989).

The scale dependence of velocity fluctuations is examined using longitudinal energy spectra. The Fourier transform of u in the x direction is denoted by $\hat{u}(k_x, y)$, where k_x is the streamwise wavenumber. With $\hat{u}^*$ representing the complex conjugate of $\hat{u}$, the energy spectrum of u is defined as $E_u(k_x, y) = \mathrm{Re}[\langle \hat{u}\hat{u}^* \rangle]$, where Re denotes the real part. As with the autocorrelation functions, a spatial average in the y direction is applied to obtain $E_u(k_x)$. Similarly, the energy spectrum of v, denoted by $E_v(k_y)$, is computed from the Fourier transform of v in the y direction, where k_y is the vertical wavenumber.

Figures 17(*a*) and 18(*a*) show E_u and E_v, respectively, together with reference results

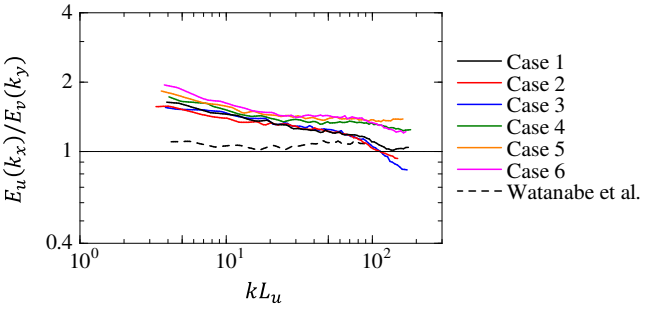

Figure 19: Ratios of energy spectra of u and v, E_u/E_v. Results for nearly HIT generated by the single jet array, evaluated 605 mm downstream of the nozzles, are shown for comparison (Watanabe *et al.* 2025).

for nearly HIT generated by the single jet array (Watanabe *et al.* 2025). The accessible wavenumber range is determined by the spatial resolution and the size of the measurement region. As discussed below, the measured range lies within the inertial subrange. In high-Reynolds-number turbulence, Kolmogorov scaling is observed in this subrange, with $E_u \sim k_x^{-5/3}$ and $E_v \sim k_y^{-5/3}$. This scaling is more clearly seen in the compensated spectra, $k_x^{5/3}E_u$ and $k_y^{5/3}E_v$, shown in figures 17(b) and 18(b). The $-5/3$ law appears as a plateau in the compensated spectra and is evident in the single-jet-array results. In contrast, the present experiments show that $k_x^{5/3}E_u$ and $k_y^{5/3}E_v$ decrease with increasing k_x and k_y, indicating a faster decay than predicted by the $-5/3$ law.

Previous studies of HIT subject to axisymmetric contraction, based on DNS and wind tunnel experiments, reported deviations in the opposite direction, where the spectra decay more slowly than the $-5/3$ law (Ayyalasomayajula & Warhaft 2006; Clay & Yeung 2016). In contrast, the present results demonstrate that axisymmetric expansion leads to faster decay. This deviation from the $-5/3$ law under axisymmetric expansion could not be assessed in previous DNS because the Reynolds numbers were too low (Lee 1989). The mean velocity gradient tensors for axisymmetric contraction and expansion can be expressed in the same form with opposite signs using a single strain-rate parameter $S > 0$, as shown in (1.2) and (1.3). These forms indicate that contraction and expansion exert opposite effects on turbulence. In this context, the faster decay in E_u and E_v observed here under axisymmetric expansion aligns with earlier findings for axisymmetric contraction.

Figure 19 shows E_u/E_v calculated at identical wavenumber values $k = k_x = k_y$, providing a measure of anisotropy at each scale. The result for the single jet array is also included for comparison (Watanabe *et al.* 2025). For the single jet array, E_u/E_v remains close to 1.05 across all wavenumbers, indicating approximate isotropy at all scales. In contrast, the present results show $E_u/E_v > 1.2$ over most wavenumbers. As E_u/E_v decreases with increasing wavenumber, the velocity fluctuations are more anisotropic at larger scales, where the influence of mean strain is more pronounced. Generally, smaller-scale turbulent motions have shorter characteristic time scales. Since the time scale of the mean strain is determined by the mean velocity gradients, it acts relatively slowly on such small-scale motions. Consequently, the direct effect of mean strain is weaker at small scales, which explains why the greatest deviation from $E_u/E_v \approx 1$ appears at larger scales.

The energy spectra describe the scale-by-scale distribution of turbulent kinetic energy in wavenumber space. A real-space equivalent is the second-order structure function, defined using the velocity difference between two points (Davidson 2015). The longitudinal structure function of u is given by $\langle(\Delta u)^2\rangle$, where $\Delta u = u'(x + r/2, y) - u'(x - r/2, y)$. In the inertial

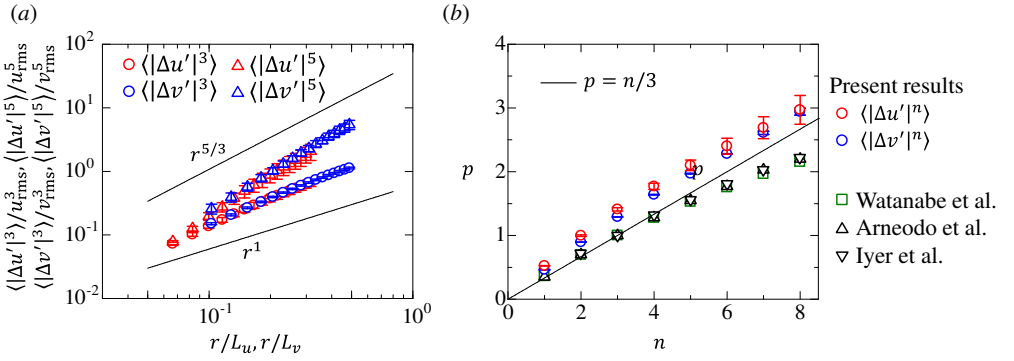

Figure 20: (*a*) Third- and fifth-order structure functions for case 4. Solid lines indicate the power laws predicted by Kolmogorov's second similarity hypothesis. (*b*) Power-law exponents p for the nth-order structure functions. Present results are compared with DNS of isotropic turbulence (Iyer *et al.* 2020) and experimental data for various turbulent flows, including jets, wakes, mixing layers, duct flows and grid turbulence (Arneodo *et al.* 1996), as well as nearly HIT generated by the same single jet array used in this study (Watanabe *et al.* 2024).

subrange, the scaling $\langle(\Delta u)^2\rangle \sim r^{2/3}$ corresponds to the spectral scaling $E_u \sim k_x^{-5/3}$. More generally, Kolmogorov's second similarity hypothesis predicts that the nth-order longitudinal structure function scales as $r^{n/3}$ (Kolmogorov 1991*a*,*b*; Davidson 2015; Tsinober 2009). Previous studies have shown that the scaling exponents deviate from $n/3$ as n increases, a phenomenon attributed to small-scale intermittency. The deviation becomes pronounced for $n \geqslant 5$ (Arneodo *et al.* 1996; Saw *et al.* 2018; Iyer *et al.* 2020). The present results for the energy spectra deviating from the $k_x^{-5/3}$ scaling imply that the structure functions deviate from the $n/3$ scaling even for small n, with the departures arising from mechanisms other than small-scale intermittency.

We evaluate the nth-order longitudinal structure function of u' as $\langle|\Delta u|^n\rangle = \langle|u'(x + r/2, y) - u'(x - r/2, y)|^n\rangle$ at $x = 0$, using ensemble averages combined with spatial averages in the y direction. Similarly, the longitudinal structure function of v' is computed at $y = 0$ as $\langle|\Delta v|^n\rangle = \langle|v'(x, y + r/2) - v'(x, y - r/2)|^n\rangle$, using ensemble averaging together with spatial averaging in the x direction. Figure 20(*a*) shows the third- and fifth-order structure functions together with the power laws $r^{n/3}$. We set the maximum separation to $r/M = 0.75$ so that $r \leqslant L_u/3$. Below this bound the structure functions exhibit clear power laws and the $-5/3$ spectral slope is observed at the corresponding wavenumbers for the single-jet-array case (Watanabe *et al.* 2024). In contrast, for turbulence subject to axisymmetric expansion, both the third- and fifth-order structure functions follow power-law behaviour but with exponents that deviate substantially from $n/3$.

Figure 20(*b*) shows the power-law exponents p of the nth-order longitudinal structure functions of u and v, obtained by least-squares fitting. The present results are compared with reference data from DNS of isotropic turbulence (Iyer *et al.* 2020) and from experiments of various flows (Arneodo *et al.* 1996). Results for nearly HIT generated by the single jet array at $Re_\lambda \approx 600$ (Watanabe *et al.* 2024), obtained with the same PIV setup, are also shown. In Watanabe *et al.* (2024), the available range of r, set by the spatial resolution and FOV of the PIV, is similar to that of the present measurements. Although the fitting range spans less than one decade, the exponents for the single jet array agree well with DNS and experimental data, confirming that the limited r range does not compromise exponent evaluation. For these reference cases, the exponents follow $p = n/3$ predicted by Kolmogorov's second

similarity hypothesis for $n \leqslant 4$, but become smaller than $n/3$ as n increases, reflecting small-scale intermittency. In contrast, the present results for turbulence subject to axisymmetric expansion yield exponents larger than $n/3$, in clear departure from other turbulent flows. The departure is similar for u and v. Since the single jet array results reproduce established turbulence data, the observed deviation is most likely due to mean strain effects. The energy spectra exhibit a faster decay than $k_x^{-5/3}$, consistent with an exponent for $n = 2$ exceeding $2/3$; indeed, $p(n = 2) = 1.1$ for $\langle|\Delta u|^n\rangle$ and 0.98 for $\langle|\Delta v|^n\rangle$ is obtained. Previous comparisons across grid turbulence, jets, mixing layers and cylinder wakes have shown that mean shear exerts little influence on the scaling of structure functions (Arneodo *et al.* 1996). Consistently, numerous experiments and numerical simulations have reported the persistence of the $-5/3$ energy spectral law in canonical turbulent shear flows (Uberoi & Freymuth 1970; Fiscaletti *et al.* 2016; Sadeghi *et al.* 2018; Takamure *et al.* 2019; Watanabe *et al.* 2019). Taken together with reports of non-$-5/3$ spectra for turbulence under axisymmetric contraction (Ayyalasomayajula & Warhaft 2006), the present findings for axisymmetric expansion suggest that mean axisymmetric strain exerts a stronger influence on structure-function scaling than mean shear.

The turbulent kinetic-energy distribution across scales can be examined using second-order structure functions, which estimate the kinetic energy contained in scales below a given separation distance (Davidson 2015). The transport equation for the second-order structure function is often utilised to assess the scale-dependent energy budget (Deissler 1992; Valente & Vassilicos 2015; Wang *et al.* 2023). This scale-by-scale energy-transport equation, originating from the Kármán–Howarth equation, contains two inviscid terms that describe interscale energy transfers: a nonlinear transfer due to turbulent fluctuations and a linear transfer due to mean velocity gradients. For the longitudinal structure functions of u and v, which are related to the longitudinal energy spectra in figures 17 and 18, the relevant nonlinear transfer terms measured on the x–y plane at $z = 0$ are

$$\Pi_{u'}(x, y, r) = -\frac{\partial\langle[u'(x^+, y) - u'(x^-, y)]^3\rangle}{\partial r}, \tag{3.5}$$

$$\Pi_{v'}(x, y, r) = -\frac{\partial\langle[v'(x, y^+) - v'(x, y^-)]^3\rangle}{\partial r}, \tag{3.6}$$

with $x^+ = x + r/2$, $x^- = x - r/2$, $y^+ = y + r/2$ and $y^- = y - r/2$, as derived in Valente & Vassilicos (2015). The corresponding linear-transfer terms are

$$\Pi_{\langle u\rangle}(x, y, r) = -\frac{\partial[\langle u\rangle(x^+, y) - \langle u\rangle(x^-, y)]\langle[u'(x^+, y) - u'(x^-, y)]^2\rangle}{\partial r}, \tag{3.7}$$

$$\Pi_{\langle v\rangle}(x, y, r) = -\frac{\partial[\langle v\rangle(x, y^+) - \langle v\rangle(x, y^-)]\langle[v'(x, y^+) - v'(x, y^-)]^2\rangle}{\partial r}. \tag{3.8}$$

Figure 21 shows these terms at $(x, y) = (0, 0)$ normalised by u_{rms}^3/L_u or v_{rms}^3/L_v. A second-order central difference is used for $\partial/\partial r$. Because small errors in the structure functions can be amplified by differentiation, we focus on the overall trends rather than precise quantification. The maximum separation for evaluation is $r = 1.8M$, close to the integral scales. Positive and negative values indicate transfers to smaller and larger scales (forward and backward transfers), respectively. Thus, $\Pi_{\langle u\rangle} > 0$ and $\Pi_{\langle v\rangle} < 0$ show that the mean velocity gradients associated with axisymmetric expansion have opposite effects: compression in the x direction gives $\langle u\rangle(x^+, y) - \langle u\rangle(x^-, y) < 0$ and hence a forward transfer with $\Pi_{\langle u\rangle} > 0$, whereas expansion in the y direction yields $\langle v\rangle(x, y^+) - \langle v\rangle(x, y^-) > 0$ and thus a backward transfer with $\Pi_{\langle v\rangle} < 0$. At large scales, the linear-transfer terms exceed the nonlinear ones. Even at $r/L_u \approx 10^{-1}$ and $r/L_v \approx 10^{-1}$ they are of comparable magnitude.

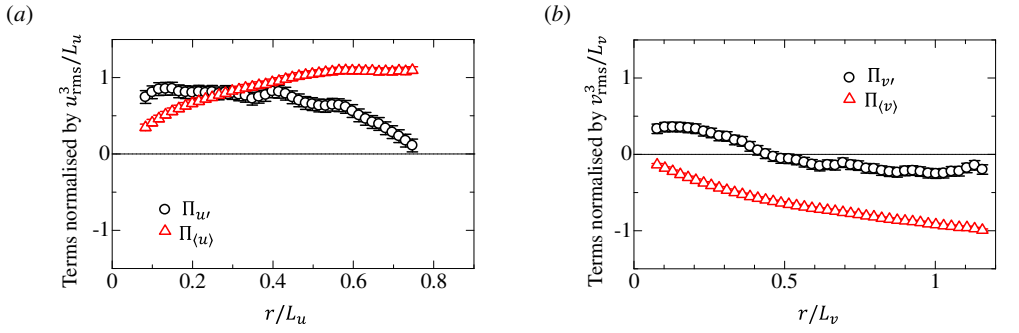

Figure 21: Linear and nonlinear longitudinal inter-scale energy transfers defined by (3.5–3.8). (*a*) Energy transfer of the x-directional velocity across scales in the x direction; (*b*) energy transfer of the y-directional velocity across scales in the y direction. The separation distance and energy-transfer terms are normalised by the integral scales and rms velocity fluctuations.

Thus, the mean velocity gradients of axisymmetric expansion alter the energy transfer across scales. The nonlinear terms also differ substantially between components. The x-component $\Pi_{u'}$ is positive, indicating forward transfer that diminishes as r approaches the integral scale, consistent with other turbulent flows (Valente & Vassilicos 2015). In general, the nonlinear term scales as $u_{\rm rms}^3/L_u$ (or $v_{\rm rms}^3/L_v$), and the normalised quantity $\Pi_{u'}/(u_{\rm rms}^3/L_u)$ is close to 1. By contrast, the y-component $\Pi_{v'}$ becomes negative at large scales, indicating that axisymmetric expansion modifies the nonlinear transfer. Deviations from the $-5/3$ law are observed in the longitudinal energy spectra of both u and v. Since axisymmetric expansion affects the inter-scale transfers of these components differently, the spectral changes are unlikely to be explained solely by the inter-scale transfers.

3.4. *Summary of turbulence statistics*

Table 1 summarises velocity statistics obtained for all experimental conditions with different test-section geometries. The dissipation scaling is used to provide an order-of-magnitude estimate of the turbulent kinetic energy dissipation rate per unit mass, $\varepsilon = A\mathcal{U}^3/\mathcal{L}$, where $\mathcal{U}$ and $\mathcal{L}$ denote the large-scale velocity and length scales. The present analysis relies on this dissipation scaling because the PIV does not resolve the smallest turbulent scales. The non-dimensional constant A varies among flows and may depend on position in the present setup, but $A = O(10^0)$ holds in most cases, including nearly HIT generated by the single jet array (Mori *et al.* 2024). We therefore take $A = 1$ for the present estimates. This approximation is used only to evaluate the orders of the Taylor microscale λ, the Kolmogorov scale η, and the turbulent Reynolds number Re_λ; accurate values of these quantities would require direct measurements of ε. The velocity and length scales are defined as $\mathcal{U} = \sqrt{2k_T/3}$ and $\mathcal{L} = (L_u{+}L_v{+}L_w)/3$, where the turbulent kinetic energy is $k_T = (\langle u'^2\rangle{+}\langle v'^2\rangle{+}\langle w'^2\rangle)/2$ and L_w is the integral scale in the z direction. With statistical equivalence in the y and z directions, we assume $\langle w'^2\rangle = \langle v'^2\rangle$ and $L_w = L_v$. The Taylor microscale and Kolmogorov scale are given by $\lambda = \sqrt{10(\mu/\rho)k_T/\varepsilon}$ and $\eta = (\mu/\rho)^{3/4}\varepsilon^{-1/4}$, respectively. The turbulent Reynolds number is $Re_\lambda = \rho\sqrt{2k_T/3}\,\lambda/\mu$. The resulting values of k_T, ε, λ, η, and Re_λ are listed in table 1.

The Kolmogorov scales are $\eta/M \approx 1\times10^{-3}$ for cases 1–3 and 0.7×10^{-3} for cases 4–6. The larger η in the former cases reflects the longer inner ducts with larger D_N, as turbulence decay increases η. Turbulence decay also enlarges the Taylor microscale, giving

λ values greater in cases 1–3 than in cases 4–6. Consistently, Re_λ is about 600 for cases 1–3 and 700 for cases 4–6. These values are sufficiently large to allow observation of the inertial subrange with the $-5/3$ law, as this scaling and its structure-function equivalent have been successfully observed in turbulence generated by the single jet array at comparable Re_λ (Mori *et al.* 2024; Watanabe *et al.* 2024). The observed deviation from the $-5/3$ law is therefore unlikely to originate from low-Reynolds-number effects. Consistently, turbulence subject to axisymmetric contraction at similar Re_λ also departs from the $-5/3$ scaling, as discussed above (Ayyalasomayajula & Warhaft 2006).

An important parameter describing the influence of mean strain on turbulence is the ratio of the strain time scale to the turbulence time scale. From (1.3), the strain rate S is evaluated from the experimental data as $S = (|A_{xx}| + 2A_{yy} + 2A_{zz})/3$, using the continuity relation $A_{zz} = -A_{xx} - A_{yy}$. The characteristic time scale of large-scale motion is defined as $T_L = \mathcal{L}/\mathcal{U}$. The normalised strain rate is expressed as ST_L, representing the ratio of T_L to the strain time scale $1/S$. Table 1 lists ST_L values for all cases. In all experiments, ST_L is close to unity, indicating that the mean strain acts on a time scale comparable to that of large-scale turbulent motions. Comparisons among cases suggest that the distance between the two opposing jet arrays, D_N, has a stronger influence on ST_L, through turbulence decay effects on T_L, than the gap length between the inner-duct exits, D_E, which affects S. Systematic experiments varying D_N would therefore be valuable for further investigations of turbulence under axisymmetric strain.

Turbulence generated by the OMJA facility exhibits $ST_L \approx 1$ while the necesarry condition for the RDT assumption to be valid is $ST_L \gg 1$. Nonetheless, several findings are qualitatively consistent with RDT. Detailed comparisons with RDT require knowledge of the total strain (distortion) experienced along mean flow trajectories. When the turbulence intensity is small, this can be inferred from spatial variations of the mean velocity using Taylor's frozen-turbulence hypothesis, as in wind-tunnel studies of axisymmetric contraction. In the present setup, however, the turbulence intensity is very high near the stagnation region, owing to the small mean velocity there and to the jet-interaction turbulence, so this approach is not suitable.

RDT for axisymmetric turbulence has been presented in previous studies (Batchelor 1946; Sreenivasan & Narasimha 1978; Hunt & Carruthers 1990). Based on these frameworks, temporal evolutions of $u_{\mathrm{rms}}/v_{\mathrm{rms}}$ and L_u/L_v under axisymmetric expansion have been derived (Pope 1985; Lee 1989). For initially HIT, RDT predicts that axisymmetric expansion induces anisotropy, increasing both $u_{\mathrm{rms}}/v_{\mathrm{rms}}$ and L_u/L_v above unity. The present measurements likewise show $u_{\mathrm{rms}}/v_{\mathrm{rms}} > 1$ and $L_u/L_v > 1$. However, RDT predicts an upper bound $u_{\mathrm{rms}}/v_{\mathrm{rms}} = \sqrt{2}$, whereas our results exceed this limit (Pope 2000). Consistently, other experiments and DNS on turbulence with axisymmetric expansion at low Reynolds numbers report greater anisotropy than RDT when the strain time scale is comparable to turbulence time scales (Liu *et al.* 1999; Choi & Lumley 2001). In addition, RDT predicts that axisymmetric strain does not modify the $-5/3$ slope of the energy spectra at high Reynolds numbers, as shown in Appendix A. This contrasts with the present results in figures 17 and 18 and with previous findings for axisymmetric contraction (Ayyalasomayajula & Warhaft 2006).

4. Conclusion

A novel turbulence facility with opposing multiple-jet arrays has been developed to investigate turbulence subject to axisymmetric expansion at large Reynolds numbers The facility employs two opposed jet generators, each producing 6×6 supersonic jets, and their interaction forms nearly HIT. The collision of the opposing turbulent flows creates a stagnation region in the

mean field, inducing axisymmetric expansion. Velocity measurements using two-component PIV have revealed both the mean strain and turbulence characteristics. The axisymmetric expansion, with mean velocity gradients satisfying $A_{xx} : A_{yy} : A_{zz} = -2 : 1 : 1$ and $A_{xx} < 0$, is uniformly established near the centre of the test section. However, the strain rate, defined as $|A_{xx}|$, varies spatially and becomes larger toward the centre along the symmetry axis.

Turbulence generated by each jet array is nearly homogeneous and isotropic, but becomes anisotropic under axisymmetric expansion. In particular, the ratios $u_{\mathrm{rms}}/v_{\mathrm{rms}}$ and L_u/L_v increase compared with those in nearly HIT generated by the single jet array. The invariant of the normalised anisotropy tensor of the Reynolds stress indicates that the flow becomes increasingly anisotropic toward the centre of the test section, reflecting the cumulative effect of mean strain. This anisotropy is qualitatively consistent with RDT predictions for initially isotropic turbulence subject to mean strain, which also predicts $u_{\mathrm{rms}}/v_{\mathrm{rms}} > 1$ and $L_u/L_v > 1$. However, the present experiments do not satisfy RDT assumptions, since the strain time scale is close to that of large-scale turbulent motions, and several deviations from RDT predictions are observed. The measured values of $u_{\mathrm{rms}}/v_{\mathrm{rms}}$ exceed the upper bound predicted by RDT. Furthermore, the energy spectra decay faster than the $-5/3$ law. Consistently, the scaling exponents of velocity structure functions deviate from the prediction based on Kolmogorov's second similarity hypothesis, even for low-order structure functions. The linear inter-scale transfer of turbulent kinetic energy due to mean velocity gradients is comparable to the non-linear contribution at large scales, inducing forward and backward transfers for u and v, respectively; nevertheless, both components exhibit similar departures from the $-5/3$ law, suggesting that the modified inter-scale transfer is not the primary cause of these departures. Since RDT does not capture these changes in the scaling laws, the results motivate further studies of the influence of mean strain on turbulence, ideally via high-Reynolds-number DNS. Unlike mean shear, which has little effect on the scaling laws (Arneodo *et al.* 1996), the present findings demonstrate that axisymmetric mean strain significantly alters turbulence properties that are otherwise considered universal.

The anomalous behaviours of the spectra and structure functions are consistent with reports for turbulence under axisymmetric contraction, where the deviation from the $-5/3$ law has been reported (Ayyalasomayajula & Warhaft 2006). The underlying cause of this departure remains unresolved and has received limited attention. Our results show that analogous deviations arise under axisymmetric expansion as well as compression, indicating a common influence of mean axisymmetric strain on inertial-range statistics. Given the central role of inertial-range scaling in turbulence theory and modelling, this deviation merits further investigation.

In the opposed multiple-jet array setup, different test section geometries enable experiments with varied strain and turbulence conditions. Extending the inner ducts increases turbulence decay before it reaches the strain region, thereby modifying its properties. Varying the gap between duct ends alters the strain rate, although it is not determined solely by this gap. The present study is limited to narrow ranges of these geometric parameters due to the number of available nozzles, constrained by the air tank volume. Nevertheless, the results demonstrate that the opposed multiple-jet array configuration offers a useful platform for parametric studies of turbulence under axisymmetric expansion, particularly when larger numbers of jets and extended test sections become available.

Acknowledgements. The authors gratefully acknowledge the technical support provided during the setup of the experimental facility by Mr. Sato, Mr. Tamaki, and Mr. Hatano of the Mechanical Engineering Group, Department of Mechanical Engineering and Science, Kyoto University. Zexu Han also acknowledges financial support from the Amano Institute of Technology Scholarship. The authors used an AI-assisted

language tool to improve readability for grammatical accuracy, spelling and clarity; all content was verified and approved by the authors, who take full responsibility for the text.

Funding. This work was supported by JSPS KAKENHI Grant Nos. JP23K22669 and JP25K01155.

Declaration of interests. The authors report no conflict of interest.

Data availability statement. The data that support the findings of this study are available from the corresponding author upon reasonable request.

Appendix A. Rapid distortion theory for turbulence subject to axisymmetric expansion

The present experiments demonstrate that axisymmetric expansion modifies the energy spectrum, which no longer follows the $-5/3$ law in the inertial subrange. This appendix examines these spectral changes in the framework of rapid distortion theory (RDT) and shows that the experimental results are inconsistent with RDT predictions. Similar discrepancies between RDT and measured spectra have also been reported in DNS and experiments of turbulence subject to axisymmetric contraction (Ayyalasomayajula & Warhaft 2006; Clay & Yeung 2016).

We briefly outline RDT for turbulence subject to axisymmetric strain, following Batchelor (1953); further details can be found in the original reference. The deformation of a fluid element $\partial x\partial y\partial z$ in initially isotropic turbulence under axisymmetric strain is given by

$$\frac{\partial x^*}{\partial x} = c, \quad \frac{\partial y^*}{\partial y} = \frac{\partial z^*}{\partial z} = \frac{1}{\sqrt{c}}, \quad \frac{\partial x_i^*}{\partial x_j} = 0 \text{ for } i \neq j, \tag{A 1}$$

where $\partial x^*\partial y^*\partial z^*$ denotes the post-deformation element and c characterises the imposed strain. x indicates the direction of the strain axis, while y and z denote the transverse directions. Axisymmetric contraction and expansion correspond to $c > 1$ and $c < 1$, respectively. An asterisk superscript $(*)$ denotes quantities in the strained state, while unstarred symbols denote those in the initial state.

The general form of the energy spectrum tensor for turbulence under arbitrary irrotational strain was derived by Batchelor (1953). Based on the spectrum tensor for axisymmetric strain given therein, the longitudinal energy spectrum in the x direction after deformation is

$$E_u^*(k_x^*) = \iint \frac{E(k)}{2\pi k^{*4}}(k_y^2 + k_z^2)\, dk_y^* dk_z^*, \tag{A 2}$$

where the strained wavenumbers k_i^* are related to the original wavenumbers k_i by

$$k_x^* = \frac{k_x}{c}, \quad k_y^* = \sqrt{c}\, k_y, \quad k_z^* = \sqrt{c}\, k_z, \tag{A 3}$$

and $E(k)$ denotes the three-dimensional energy spectrum of the initial isotropic state with wavenumber k.

The strain effects can be evaluated with RDT by numerically integrating (A 2) using a prescribed form of $E(k)$. Here we adopt the model spectrum of Pope (2000):

$$E(k) = C\varepsilon^{2/3}k^{-5/3} f_L(kL_k) f_\eta(k\eta), \tag{A 4}$$

$$f_L(kL_k) = \left(\frac{kL_k}{\sqrt{(kL_k)^2 + c_L}}\right)^{5/3+p_0}, \tag{A 5}$$

$$f_\eta(k\eta) = \exp\left\{-\beta\left(\left[(k\eta)^4 + c_\eta^4\right]^{1/4} - c_\eta\right)\right\}, \tag{A 6}$$

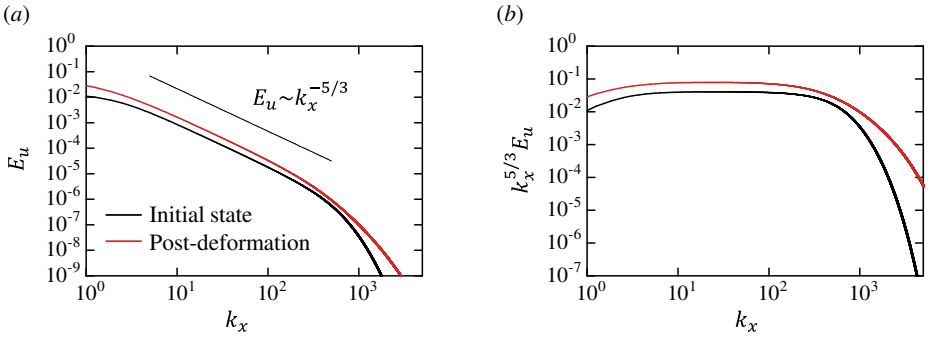

Figure 22: Longitudinal energy spectra of x-directional velocity fluctuations, $E_u(k_x)$, before and after deformation due to axisymmetric expansion. The post-deformation spectrum is computed using RDT with (A 2).

where $C = 1.5$ is the Kolmogorov constant, ε the energy dissipation rate, L_k the integral length scale and η the Kolmogorov length scale. The integral scale is defined as $L_k = k_T^{3/2}/\varepsilon$ with the turbulent kinetic energy k_T. This definition is different from the integral scales in § 3.3, where the integration of autocorrelation functions yield the integral scales. The Taylor microscale is $\lambda = \sqrt{10 k_T \nu/\varepsilon}$, with ν the kinematic viscosity, and the turbulent Reynolds number is $Re_\lambda = \sqrt{2k_T/3}\,\lambda/\nu$. We consider an initial isotropic turbulence with rms velocity $\sqrt{2k_T/3} = 1$ and integral scale $L = 1$ in arbitrary units. Specifying Re_λ then fixes ν and ε, which are used to evaluate $E(k)$.

The post-deformation spectra are computed from (A 2) for $Re_\lambda = 600$ with $c = 0.25$. We have confirmed that varying c does not affect the shape of the energy spectra. Figure 22(a) compares the longitudinal energy spectrum of the x-directional velocity before and after deformation. The post-deformation spectrum is shifted upward relative to the initial isotropic state, indicating enhanced velocity fluctuations, consistent with the present experimental observations. In both pre- and post-deformation spectra, the inertial-range scaling $E_u \sim k_x^{-5/3}$ is clearly observed. This is further demonstrated in the compensated spectra $k_x^{5/3} E_u$ in figure 22(b), where the plateau region is nearly identical for both cases. Although not shown, axisymmetric contraction with $c > 1$ exhibits the same trend, with negligible deformation effects on the $k_x^{-5/3}$ scaling. These RDT predictions contradict the present results for axisymmetric expansion and previous findings for axisymmetric contraction (Ayyalasomayajula & Warhaft 2006; Clay & Yeung 2016), suggesting that nonlinear effects play a significant role in both strain types.

REFERENCES

Alhareth, A. A., Mugundhan, V., Langley, K. R. & Thoroddsen, S. T. 2024 Coherent turbulent structures in a rapid contraction. *J. Fluid Mech.* **1000**, A63.

Arneodo, A., Baudet, C., Belin, F., Benzi, R., Castaing, B., Chabaud, B., Chavarria, R., Ciliberto, S., Camussi, R., Chilla, F. & others 1996 Structure functions in turbulence, in various flow configurations, at Reynolds number between 30 and 5000, using extended self-similarity. *Europhys. Lett.* **34** (6), 411.

Ayyalasomayajula, S. & Warhaft, Z. 2006 Nonlinear interactions in strained axisymmetric high-Reynolds-number turbulence. *J. Fluid Mech.* **566**, 273–307.

Batchelor, G. K. 1946 The theory of axisymmetric turbulence. *Proc. Roy. Soc. A.* **186** (1007), 480–502.

Batchelor, G. K. 1953 *The theory of homogeneous turbulence*. Cambridge university press.

Batchelor, G. K. & Proudman, I. 1954 The effect of rapid distortion of a fluid in turbulent motion. *Quart. J. Mech. Appl. Math.* **7** (1), 83–103.

Bewley, G. P., Chang, K. & Bodenschatz, E. 2012 On integral length scales in anisotropic turbulence. *Phys. Fluids* **24** (6), 061702.

Brown, M. L., Parsheh, M. & Aidun, C. K. 2006 Turbulent flow in a converging channel: effect of contraction and return to isotropy. *J. Fluid Mech.* **560**, 437–448.

Chandrasekhar, S. 1950 The theory of axisymmetric turbulence. *Proc. Roy. Soc. A.* **242** (855), 557–577.

Chen, J. U. N., Meneveau, C. & Katz, J. 2006 Scale interactions of turbulence subjected to a straining–relaxation–destraining cycle. *J. Fluid Mechanics* **562**, 123–150.

Choi, K.-S. & Lumley, J. L. 2001 The return to isotropy of homogeneous turbulence. *J. Fluid Mech.* **436**, 59–84.

Clay, M. P. & Yeung, P. K. 2016 A numerical study of turbulence under temporally evolving axisymmetric contraction and subsequent relaxation. *J. Fluid Mech.* **805**, 460–493.

Clemens, N. T. & Mungal, M. G. 1991 A planar Mie scattering technique for visualizing supersonic mixing flows. *Exp. Fluids* **11** (2-3), 175–185.

Comte-Bellot, G. & Corrsin, S. 1966 The use of a contraction to improve the isotropy of grid-generated turbulence. *J. Fluid Mech.* **25** (4), 657–682.

Davidson, P. A. 2010 On the decay of Saffman turbulence subject to rotation, stratification or an imposed magnetic field. *J. Fluid Mech.* **663**, 268–292.

Davidson, P. A. 2013 *Turbulence in rotating, stratified and electrically conducting fluids*. Cambridge University Press.

Davidson, P. A. 2015 *Turbulence: An Introduction for Scientists and Engineers*. Oxford Univ. Pr.

Davidson, P. A., Okamoto, N. & Kaneda, Y. 2012 On freely decaying, anisotropic, axisymmetric Saffman turbulence. *J. Fluid Mech.* **706**, 150–172.

Deissler, R. G. 1992 Effects of inhomogeneity and of shear flow in weak turbulent fields. *Phys. Fluids* **4** (10), 1187–1198.

Ertunç, Ö. & Durst, F. 2008 On the high contraction ratio anomaly of axisymmetric contraction of grid-generated turbulence. *Phys. Fluids* **20** (2), 025103.

Fiscaletti, D., Elsinga, G. E., Attili, A., Bisetti, F. & Buxton, O. R. H. 2016 Scale dependence of the alignment between strain rate and rotation in turbulent shear flow. *Phys. Rev. Fluids* **1** (6), 064405.

Foelsch, K. 1949 The analytical design of an axially symmetric Laval nozzle for a parallel and uniform jet. *J. Aeronaut. Sci.* **16** (3), 161–166.

Griffin, K. P., Wei, N. J., Bodenschatz, E. & Bewley, G. P. 2019 Control of long-range correlations in turbulence. *Exp. Fluids* **60**, 1–14.

Gylfason, A., Lee, C., Perlekar, P. & Toschi, F. 2011 Direct numerical simulation on strained turbulent flows and particles within. *J. Phys.* **318** (5), 052003.

Hassanian, R., Helgadóttir, Á., Bouhlali, L. & Riedel, M. 2023 An experiment generates a specified mean strained rate turbulent flow: Dynamics of particles. *Phys. Fluids* **35** (1), 015124.

Hunt, J. C. R. & Carruthers, D. J. 1990 Rapid distortion theory and the 'problems' of turbulence. *J. Fluid Mech.* **212**, 497–532.

Hussain, A. K. M. F. & Ramjee, V. 1976 Effects of the axisymmetric contraction shape on incompressible turbulent flow. *J. Fluids Eng.* **98** (1), 58–68.

Isaza, J. C., Salazar, R. & Warhaft, Z. 2014 On grid-generated turbulence in the near-and far field regions. *J. Fluid Mech.* **753**, 402–426.

Iyer, K. P., Sreenivasan, K. R. & Yeung, P. K. 2020 Scaling exponents saturate in three-dimensional isotropic turbulence. *Phys. Rev. Fluids* **5** (5), 054605.

Kang, H. S. & Meneveau, C. 2008 Experimental study of an active grid-generated shearless mixing layer and comparisons with large-eddy simulation. *Phys. Fluids* **20** (12), 125102.

Keffer, J. F. 1965 The uniform distortion of a turbulent wake. *J. Fluid Mech.* **22** (1), 135–159.

Kitamura, T., Nagata, K., Sakai, Y., Sasoh, A., Terashima, O., Saito, H. & Harasaki, T. 2014 On invariants in grid turbulence at moderate Reynolds numbers. *J. Fluid Mech.* **738**, 378–406.

Kolmogorov, A. N. 1991*a* Dissipation of energy in the locally isotropic turbulence. *Proc. Roy. Soc. A* **434** (1890), 15–17.

Kolmogorov, A. N. 1991*b* The local structure of turbulence in incompressible viscous fluid for very large Reynolds numbers. *Proc. Roy. Soc. A* **434** (1890), 9–13.

Kouchi, T., Fukuda, S., Miyai, S., Nagata, Y. & Yanase, S. 2019 Acetone-condensation nano-particle image velocimetry in a supersonic boundary layer. In *AIAA Scitech 2019 Forum*, p. 1821.

Krogstad, P.-Å. & Davidson, P. A. 2012 Near-field investigation of turbulence produced by multi-scale grids. *Phys. Fluids* **24** (3), 035103.

Lee, M. J. 1989 Distortion of homogeneous turbulence by axisymmetric strain and dilatation. *Phys. Fluids* **1** (9), 1541–1557.

Li, S., Li, J., Yang, Q., Li, T., Wang, P. & Huang, H. 2024 Three-dimensional distortion of free-stream turbulence with the leading-edge stagnation point of an elongated bluff body. *Phys. Fluids* **36** (12), 125177.

Lindborg, E. 1995 Kinematics of homogeneous axisymmetric tubulence. *J. Fluid Mech.* **302**, 179–201.

Liu, S., Katz, J. & Meneveau, C. 1999 Evolution and modelling of subgrid scales during rapid straining of turbulence. *J. Fluid Mech.* **387**, 281–320.

Matsushima, T., Nagata, K. & Watanabe, T. 2021 Wavelet analysis of shearless turbulent mixing layer. *Phys. Fluids* **33** (2), 025109.

Mori, T., Watanabe, T. & Nagata, K. 2024 Nearly homogeneous and isotropic turbulence generated by the interaction of supersonic jets. *Exp. Fluids* **65** (4), 47.

Morikawa, K., Urano, S., Sanada, T. & Saito, T. 2008 Turbulence modulation induced by bubble swarm in oscillating-grid turbulence. *J. Power Energy Syst.* **2** (1), 330–339.

Morize, C. & Moisy, F. 2006 Energy decay of rotating turbulence with confinement effects. *Phys. Fluids* **18** (6), 065107.

Mugundhan, V., Pugazenthi, R. S., Speirs, N. B., Samtaney, R. & Thoroddsen, S. T. 2020 The alignment of vortical structures in turbulent flow through a contraction. *J. Fluid Mech.* **884**, A5.

Nakamura, K., Matsushima, T., Zheng, Y., Nagata, K. & Watanabe, T. 2022 Large-and small-scale characteristics in a temporally developing shearless turbulent mixing layer. *Phys. Fluids* **34** (11), 115117.

Nakamura, K., Watanabe, T. & Nagata, K. 2023 Turbulent/turbulent interfacial layers of a shearless turbulence mixing layer in temporally evolving grid turbulence. *Phys. Fluids* **35** (4), 045117.

Nieuwstadt, F. T .and Westerweel, J. & Boersma, B. 2016 *Introduction to Theory and Applications of Turbulent Flows*. Springer.

Pack, D. C. 1950 A note on Prandtl's formula for the wave-length of a supersonic gas jet. *Q. J. Mech. Appl. Math.* **3** (2), 173–181.

Pizzaia, A. & Rossmann, T. 2018 Effect of boundary layer thickness on transverse sonic jet mixing in a supersonic turbulent crossflow. *Phys. Fluids* **30** (11), 115104.

Pope, S. B. 1985 PDF methods for turbulent reactive flows. *Prog. Energy Combust. Sci.* **11** (2), 119–192.

Pope, S. B. 2000 *Turbulent Flows*. Cambridge Univ. Pr.

Raffel, M., Willert, C. E., Scarano, F., Kähler, C. J., Wereley, S. T. & Kompenhans, J. 2018 *Particle image velocimetry: a practical guide*. springer.

Rogallo, R. S. 1981 *Numerical experiments in homogeneous turbulence*. National Aeronautics and Space Administration.

Sadeghi, H., Oberlack, M. & Gauding, M. 2018 On new scaling laws in a temporally evolving turbulent plane jet using Lie symmetry analysis and direct numerical simulation. *J. Fluid Mech.* **854**, 233–260.

Sagaut, P. & Cambon, C. 2018 *Homogeneous turbulence dynamics*. Springer.

Saw, E.-W., Debue, P., Kuzzay, D., Daviaud, F. & Dubrulle, B. 2018 On the universality of anomalous scaling exponents of structure functions in turbulent flows. *J. Fluid Mech.* **837**, 657–669.

Sjögren, T. & Johansson, A. V. 1998 Measurement and modelling of homogeneous axisymmetric turbulence. *J. Fluid Mech.* **374**, 59–90.

Skrbek, L. & Stalp, S. R. 2000 On the decay of homogeneous isotropic turbulence. *Phys. Fluids* **12** (8), 1997–2019.

Sreenivasan, K. R. & Narasimha, R. 1978 Rapid distortion of axisymmetric turbulence. *J. Fluid Mech.* **84** (3), 497–516.

Takamure, K., Sakai, Y., Ito, Y., Iwano, K. & Hayase, T. 2019 Dissipation scaling in the transition region of turbulent mixing layer. *Int. J. Heat Fluid Flow* **75**, 77–85.

Tan, S., Xu, X., Qi, Y. & Ni, R. 2023 Scalings and decay of homogeneous, nearly isotropic turbulence behind a jet array. *Phys. Rev. Fluids* **8** (2), 024603.

Theunissen, R. 2010 Adaptive image interrogation for PIV: Application to compressible flows and interfaces. *Ph.D. thesis, TU Delft, Delft University of Technology* .

Thoroddsen, S. T. & Van Atta, C. W. 1995 The effects of a vertical contraction on turbulence dynamics in a stably stratified fluid. *J. Fluid Mech.* **285**, 371–406.

Tsinober, A. 2009 *An informal conceptual introduction to turbulence*. Springer.

Uberoi, M. S. 1956 Effect of wind-tunnel contraction on free-stream turbulence. *J. Aeronaut. Sci.* **23** (8), 754–764.

Uberoi, M. S. & Freymuth, P. 1970 Turbulent energy balance and spectra of the axisymmetric wake. *Phys. Fluids* **13** (9), 2205–2210.

Valente, P. C. & Vassilicos, J. C. 2015 The energy cascade in grid-generated non-equilibrium decaying turbulence. *Phys. Fluids* **27** (4).

Veeravalli, S. & Warhaft, Z. 1989 The shearless turbulence mixing layer. *J. Fluid Mech.* **207**, 191–229.

Wang, M., Yurikusa, T., Iwano, K., Sakai, Y., Ito, Y., Zhou, Y. & Hattori, Y. 2023 Scale-by-scale analysis of interscale scalar transfer in grid turbulence with mean scalar gradient. *Phys. Fluids* **35** (4), 045153.

Watanabe, T., Inagaki, T., Mori, T., Ishizawa, K. & Nagata, K. 2025 Direct numerical simulations of the interaction of temporally evolving circular jets. *J. Fluid Mech.* **1009**, A68.

Watanabe, T., Mori, T., Ishizawa, K. & Nagata, K. 2024 Scale dependence of local shearing motion in decaying turbulence generated by multiple-jet interaction. *J. Fluid Mech.* **997**, A14.

Watanabe, T., Zhang, X. & Nagata, K. 2019 Direct numerical simulation of incompressible turbulent boundary layers and planar jets at high Reynolds numbers initialized with implicit large eddy simulation. *Comput. Fluids* **194**, 104314.

Watanabe, T., Zheng, Y. & Nagata, K. 2022 The decay of stably stratified grid turbulence in a viscosity-affected stratified flow regime. *J. Fluid Mech.* **946**, A29.

Westerweel, J. 1997 Fundamentals of digital particle image velocimetry. *Meas. Sci. Technol.* **8** (12), 1379.

Westerweel, J. & Scarano, F. 2005 Universal outlier detection for PIV data. *Exp. Fluids* **39** (6), 1096–1100.

Zusi, C. J. & Perot, J. B. 2013 Simulation and modeling of turbulence subjected to a period of uniform plane strain. *Phys. Fluids* **25** (11), 110819.

Zusi, C. J. & Perot, J. B. 2014 Simulation and modeling of turbulence subjected to a period of axisymmetric contraction or expansion. *Phys. Fluids* **26** (11), 115103.